Mode Vector Modulation: Extending Stokes Vector Modulation to Higher Dimensions

Jaroslaw Kwapisz , Member, IEEE, Ioannis Roudas , Senior Member, IEEE, and Eric Fink

Abstract—We examine the scalability of Stokes vector modulation (SVM) to higher-dimensional Stokes spaces in order to decrease the energy consumption of optical links. We propose and study mode vector modulation (MVM), a new multidimensional SVM scheme for transmission over multimode/multicore optical fibers or free-space modes. MVM can be demodulated using a digital polarimetric direct-detection (DD) receiver that is an extension of the original single-mode Stokes vector receiver to multimode links. This paper focuses on the MVM transceiver architecture, the back-to-back performance of optically-preamplified DD MVM receivers, the optimized geometric shaping of the MVM constellation, and the related bit-to-symbol mapping. We show that MVM DD outperforms conventional single-mode, direct-detectioncompliant, digital modulation formats by several dB in terms of receiver sensitivity and the SNR gain increases with the number of spatial degrees of freedom (SDOFs) N. At the conclusion of the study, we consider the potential application of MVM as a substitute for M-ary pulse amplitude modulation (M-PAM) or M-SVM in short-haul optical links and evaluate its benefits and drawbacks.

Index Terms—Data center interconnects, polarization shift keying (PolSK), Stokes vector modulation (SVM), direct detection (DD), short-haul optical communications, space division multiplexing (SDM).

I. INTRODUCTION

PECTRALLY-EFFICIENT modulation formats for high-capacity, short-haul optical communications systems [1], [2], in conjunction with advanced direct-detection receivers, have become one of the most active research areas in contemporary optical communications.

Low cost, low energy consumption, and high spectral efficiency are desirable features for short-haul applications [3]. To satisfy these requirements, commercially-available 400G-Ethernet optical interconnects for various distances currently use several parallel fiber lanes (or separate wavelengths), each carrying either binary intensity modulation (IM) or quaternary

Manuscript received 23 March 2023; revised 31 August 2023; accepted 30 September 2023. Date of publication 17 November 2023; date of current version 18 March 2024. This work was supported in part by the National Science Foundation under Grant 1911183 and in part by the Air Force Research Laboratory under Grant FA8750-20-1-1004 PCSN T04257. (Corresponding author: Ioannis Roudas.)

Jaroslaw Kwapisz and Eric Fink are with the Department of Mathematical Sciences, Montana State University, Bozeman, MT 59717 USA (e-mail: jkwapisz@montana.edu; eric.fink@montana.edu).

Ioannis Roudas is with the Department of Electrical and Computer Engineering, Montana State University, Bozeman, MT 59717 USA (e-mail: ioannis.roudas@montana.edu).

Color versions of one or more figures in this article are available at https://doi.org/10.1109/JLT.2023.3333801.

Digital Object Identifier 10.1109/JLT.2023.3333801

pulse amplitude modulation (4-PAM), and direct-detection (DD) receivers [4], [5], [6], [7].

Given the forecasted exponential increase in data traffic in the near future due to broadband applications [8], to accommodate traffic demands, it will be important to keep increasing the spectral efficiency per fiber lane or per wavelength channel of short-haul optical links in an energy-efficient manner. The main disadvantage of M-PAM is that, at the amplified spontaneous emission (ASE) noise limit, its energy consumption scales quadratically with the number of amplitude levels M [9] since the M-PAM constellation is one-dimensional. Therefore, it would be beneficial to adopt advanced multi-dimensional modulation formats, which are preferably still amenable to direct detection but offer a better spectral efficiency-energy efficiency trade-off compared to M-PAM.

Looking forward, we anticipate that it will be necessary to modulate additional attributes of the optical wave other than the amplitude, e.g., the phase or the polarization, in order to increase spectral efficiency beyond today's values while keeping energy consumption at acceptable levels. Consequently, it will be necessary to recover the information imprinted in the electric field of the optical wave using either direct-detection-based interferometry [10], direct-detection-based polarimetry [11], self-homodyning [2], [12], [13], [14], [15], or low-cost coherent detection [16], [17], [18], [19], [20], [21]. In this paper, we focus our attention exclusively on digital polarization modulation formats in conjunction with direct-detection-based polarimetry.

Polarization shift keying (PolSK) was first studied in the late 1980s [22], [23] and early 1990s [24], [25], [26] before later falling into obscurity. It was recently revived as a subset of Stokes vector modulation (SVM) [27], [28], [29], [30], [31], [32], [33], [34], [35], [36], [37], [38], [39], [40], [41], [42], [43], [44], [45], [46], [47] when research in direct-detection systems was rekindled. This renewed interest in digital polarization modulation formats has been fueled by the maturity and low cost of integrated photonic components and the possibility of using adaptive electronic equalizers in the direct-detection optical receivers to compensate for polarization rotations introduced by short optical fibers¹.

SVM allows for more power-efficient signaling than M-PAM. This is achieved by spreading the constellation points

¹Other applications of the Stokes space formalism were also proposed in combination with various modulation formats [48], [49], [50], [51], [52], [53], [54], as well as in combination with digital signal processing (DSP) [55], [56], [57], [58], [59].

0733-8724 © 2023 IEEE. Personal use is permitted, but republication/redistribution requires IEEE permission. See https://www.ieee.org/publications/rights/index.html for more information.

Mode vector modulation/Direct detection SER Tx/Rx Decision Geometric B₂S **Basic formalism** architecture criterion constellation mapping shaping Jones/Stokes notation UB MVM Tx MVM Rx MAP objective Numerical function optimization Asymptotics Signal set Objective Numerical function optimization Cascaded Parallel Complexity ML BER UB Y-iunctions simulated annealing Gradient Thomson Quadratic Linear descent **Tammes** SER UB

Fig. 1. Hierarchical organization of the paper (Abbreviations: MVM=Mode vector modulation, Tx=transmitter, Rx=receiver, UB=Union Bound, BER=bit error rate, SER=symbol error rate, MAP= maximum a posteriori, ML=maximum likelihood, MZM=Mach-Zehnder modulator, B2S mapping=bit-to-symbol mapping).

in the three-dimensional Stokes space, as opposed to the one-dimensional M-PAM signal space.

To further increase the energy-efficiency of SVM formats, a transition to a higher-dimensional Stokes space is necessary, which can be achieved by using SVM together with few-mode fibers (FMFs) and multicore fibers (MCFs) or free-space modes [53]. We call this novel, multi-dimensional version of SVM *mode vector modulation (MVM)*.

SVM and MVM are spatial modulation formats [60]. It is worth mentioning here that several papers studied spatial modulation formats for *coherent* optical communication systems over MCFs. For instance, Eriksson et al. [61] analyzed multidimensional position modulation (MDPM) with multiple pulses per frame (*K*-over-*L*-MDPM) in combination with quadrature phase shift keying (QPSK), polarization-multiplexed QPSK (PM-QPSK) and polarization-switched QPSK (PS-QPSK) to increase both the spectral efficiency and the asymptotic energy efficiency compared to conventional modulation formats. In companion papers, Puttnam et al. [62], [63], [64] reviewed spatial modulation formats for high-capacity coherent or self-homodyne optical systems using homogeneous multicore fibers.

In this article, we study, for the first time, short-haul optical interconnects using MVM along with optically-preamplified direct-detection receivers. A visual abstract of the paper is given in Fig. 1. In the remainder of the paper, we elaborate on the following topics:

- 1) An overview of MVM along with the necessary mathematical formalism, notation, and simplifying assumptions (Section II);
- 2) The optimal MVM transceiver architecture (Section III);
- The performance limits of MVM optically-preamplified direct-detection receivers using both Monte Carlo simulation and a new analytical formula that we derived for the union bound (Section IV);
- 4) The design of geometrically-shaped constellations with arbitrary cardinality M, obtained by numerical optimization of various objective functions using the method of gradient descent (Section V);

- 5) The bit-to-symbol mapping optimization using simulated annealing (Section VI);
- The investigation of various constellation designs and bit encodings using analytical and numerical methods (Section VII);
- 7) The use of simplex MVM constellations based on symmetric, informationally complete, positive operator-valued measure (SIC-POVM) vectors [65] (Section VII);
- 8) A comparative analysis of MVM DD against alternative modulation formats used in short-haul optical links (Section VIII).

Early results on the above topics were presented in [66], [67], [68], [69], [70], [71].

II. MODE VECTOR MODULATION OVERVIEW

A. MVM Signal Representation

As mentioned before, MVM can be used together with multimode and multicore fibers, as well as for free-space transmission. In this section, for the description of the operation of the MVM transceiver, without loss of generality, we examine the special case of MVM transmission over an ideal homogeneous multicore fiber with identical single-mode cores and negligible differential group delay among cores.

We assume that we select a subset of K single-mode cores of the multicore fiber (Fig. 2). MVM consists in sending optical pulses over all these cores simultaneously with the same shape but different amplitudes and initial phases (Fig. 3). Similar to SVM over single-mode fibers (SMFs), wherein the optical wave can be analyzed in two orthogonal states of polarization, e.g., x and y, the composite optical wave of MVM over a homogeneous single-mode-core multicore fiber can be described by $N=2\,K$ orthogonal states of polarization, e.g., x and y in each core.

The mathematical representation of the MVM signals at the fiber input is written as

$$\mathbf{E}_m(t) = A_m \exp\left(\iota \phi_m\right) g(t) |s_m\rangle,\tag{1}$$

where m = 1, ..., M, A_m and ϕ_m denote the common amplitude and phase, respectively, g(t) is a real function describing

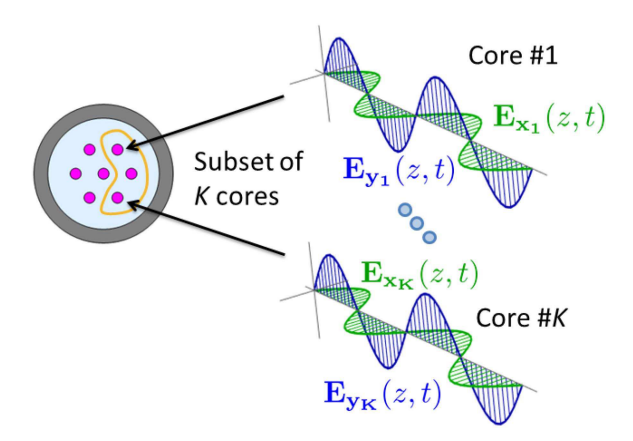


Fig. 2. MVM over homogeneous MCFs with single-mode cores.

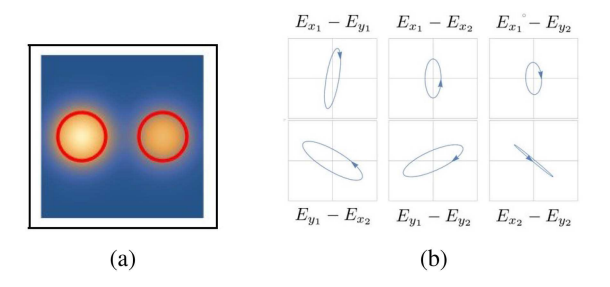


Fig. 3. (a) Intensity plot and (b) Polarization ellipses of an MVM signal propagating over an ideal homogeneous two-core MCF with identical uncoupled single-mode cores.

the pulse shape, and $|s_m\rangle$ is a generalized unit Jones vector collecting the complex excitations of the cores, i.e., the amplitudes and phases of electric fields of the optical waves [72], [73], [74].

The signal energy \mathcal{E}_s is given by [9]

$$\mathcal{E}_s := \frac{1}{2} \int_{-\infty}^{\infty} \mathbf{E}_m(t)^{\dagger} \mathbf{E}_m(t) dt = \frac{A_m^2}{2} \int_{-\infty}^{\infty} g(t)^2 dt = \frac{A_m^2}{2} \mathcal{E}_g,$$
(2)

where \dagger denotes the adjoint (i.e., conjugate transpose) of a matrix and \mathcal{E}_g denotes the pulse energy defined as

$$\mathcal{E}_g := \int_{-\infty}^{\infty} g(t)^2 dt. \tag{3}$$

In the remainder of the article, without loss of generality, we consider that the common amplitude A_m and phase ϕ_m in (1) are constant. In other words, we focus exclusively on a special case of MVM that is a generalization of PolSK to higher dimensions.

In PolSK MVM, we modulate all available spatial degrees of freedom (SDOFs) to transmit an MVM symbol. In the SVM literature, however, alternative modulation and demodulation strategies have been proposed, which could be applied to MVM as well. For instance, it is possible to transmit an unmodulated carrier on one of the SDOFs [29], [30], [31], [53] and use this carrier to perform self-homodyning of the remaining SDOFs. This technique takes advantage of a fraction (N-1)/N of the available capacity. However, for large N, the capacity loss is immaterial. Furthermore, on the upside, this self-homodyne

technique enables the use of more spectrally-efficient modulation formats, such as 16-QAM, and it is amenable to electronic chromatic dispersion compensation. The merits of such alternative MVM schemes vis-à-vis the PolSK MVM examined here are outside of the scope of this article and will be part of future research.

B. Mathematical Notation

Throughout the paper, we follow the conventions of [73], [74], [75], where Dirac's ket vectors represent both unit and non-unit vectors in the generalized Jones space, while hats indicate unit vectors and arrows indicate non-unit vectors in the generalized Stokes space.

We can parameterize a unit Jones vector $|s\rangle$, up to phase, using 2N-2 hyperspherical coordinates [74], i.e.,

$$|s\rangle := \left[\cos\phi_1, \sin\phi_1\cos\phi_2 e^{i\theta_1}, \sin\phi_1\sin\phi_2\cos\phi_3 e^{i\theta_2}, \dots, \\ \sin\phi_1 \cdots \cos\phi_{N-1} e^{i\theta_{N-2}}, \sin\phi_1 \cdots \sin\phi_{N-1} e^{i\theta_{N-1}}\right]^T,$$
(4)

where the superscript T indicates transposition.

Unit Jones vectors up to phase are often represented by generalized real unit Stokes vectors \hat{s} in a higher-dimensional real vector space \mathbb{R}^{N^2-1} . Generalized unit Stokes vectors are defined by the quadratic form [74]

$$\hat{s} := C_N \langle s | \mathbf{\Lambda} | s \rangle, \tag{5}$$

where Λ denotes the generalized Gell-Mann matrix vector and C_N denotes the normalization coefficient [74],

$$C_N := \sqrt{\frac{N}{2(N-1)}}. (6)$$

From the generalized Stokes vector definition (5), we notice that the dimensionality of the generalized Stokes space grows quadratically with the number of spatial and polarization modes N in MMFs/MCFs. Therefore, instead of using SVM DD in conjunction with the conventional 3D Stokes space, we can generate more energy-efficient constellations by spreading the constellation points in the generalized Stokes space.

Also notice that the N^2-1 components of \hat{s} are functions of the 2N-2 hyperspherical coordinates of $|s\rangle$ in (4) and, therefore, are interdependent.

For each unit Jones vector $|s\rangle$, we can define the associated projection operator $\mathbf{S}:=|s\rangle\langle s|$, which represents a mode filter, i.e., the equivalent of a polarizer in the two-dimensional case. This projection operator can be expressed in terms of the identity matrix and the generalized Gell-Mann matrices [74]

$$\mathbf{S} = \frac{1}{N} \mathbf{I}_N + \frac{1}{2C_N} \hat{\mathbf{s}} \cdot \mathbf{\Lambda}. \tag{7}$$

By rearranging the terms in (7), we obtain

$$\hat{s} \cdot \mathbf{\Lambda} = 2C_N \left(\mathbf{S} - \frac{1}{N} \mathbf{I}_N \right). \tag{8}$$

From (8), we see that Stokes vectors arise as coefficients with respect to a fixed Gell-Mann basis for the *trace-neutralized dyad* $\mathbf{S} - \frac{1}{N}\mathbf{I}_N$, assuming $\langle s|s \rangle = 1$.

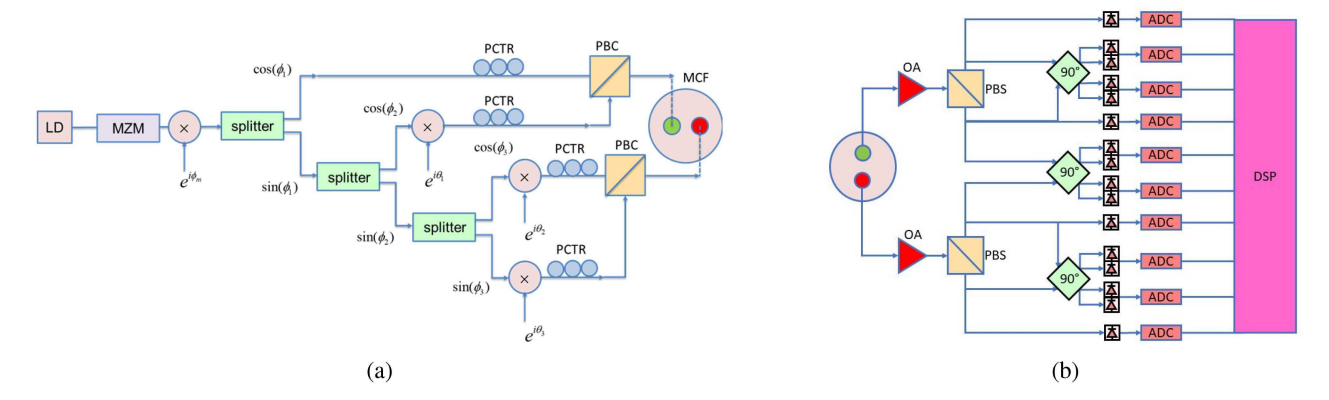


Fig. 4. Schematic of the proposed (a) MVM transmitter and (b) Optically-preamplified MVM DD receiver for an ideal homogeneous two-core MCF with identical uncoupled single-mode cores. Symbols: LD=laser diode, MZM=Mach-Zehnder modulator, OA=optical amplifier and matched optical filter, PCTR=polarization controller, PBC/S=polarization beam combiner/splitter, 90° -90°-optical hybrid, ADC=Analog-to-digital converter. (Condition: N=4.)

In the remainder of the article, we will use the Jones vector up to phase $e^{\iota\theta}|s\rangle$, the dyad $\mathbf{S}=|s\rangle\langle s|$, and the Stokes vector \hat{s} interchangeably, depending on which one is more convenient. In particular, even when we use Jones vectors to represent points in a constellation, since we consider noncoherent detection, we refer to it as a generalized Stokes constellation.

C. Simplifying Assumptions

In Section IV, we will analytically calculate the back-to-back performance of M-ary MVM over N spatial and polarization degrees of freedom in the ASE noise-limited regime. For mathematical tractability, we neglect all transmission impairments other than ASE noise and random carrier phase shifts, as well as transceiver imperfections and implementation penalties. These simplifying assumptions are justified in the sense that we want to quantify the ultimate potential of MVM for use in optical interconnects.

Nevertheless, it is worth discussing upfront about the anticipated impact of the most prominent transmission effects.

In general, the extension of SVM to MVM requires similar conditions for transmission, i.e., negligible chromatic dispersion (CD), modal dispersion (MD), and mode-dependent loss (MDL), or their full compensation, either in the optical or the electronic domain, before making decisions on the received symbols at the receiver. Let us briefly contemplate how feasible it would be to satisfy these requirements in the case of practical homogeneous multicore fibers with single-mode cores.

As a starting point, consider transmission over homogeneous MCFs with uncoupled or weekly-coupled single-mode cores. These fibers typically exhibit static and dynamic intercore skew [62]. The static differential mode group delay (DMGD) spread is on the order of 0.5 ns/km and grows linearly with the transmission distance. The DMGD spread due to the dynamic component of the intercore skew is of the order of 0.5 ps/km and also grows linearly with the transmission distance.

On the other hand, coupled-core MCFs exhibit modal dispersion and strong coupling among their supermodes and the DMGD grows with the square root of the transmission distance [76], [77]. From published values based on the characterization of several coupled-core MCFs used in MDM experiments, we conclude that the MD coefficient is currently on the order of $3\text{-}6\,\text{ps}/\sqrt{\text{km}}$. These values are much higher than typical polarization mode dispersion (PMD) coefficient values for single-mode fibers (SMFs), e.g., from the data sheet of Corning SMF-28 Ultra optical fiber [78], we notice that the PMD coefficient is less than $0.1\,\text{ps}/\sqrt{\text{km}}$.

Transmission impairments can be compensated using a combination of optical and electronic techniques at the transmitter and the receiver. These techniques are out of the scope of this article, since we are interested in the back-to-back performance of MVM systems, and will be part of future work. For simplicity, in the depiction of the optically-preamplified MVM DD receiver in Fig. 4(b), we assume ideal optical post-compensation of all transmission impairments.

III. TRANSCEIVER DESIGN

In Fig. 4(a), we draw the block diagram of an MVM transmitter for an ideal homogeneous multicore fiber with two identical single-mode cores (N=4). The schematic shows the optical components required for a single wavelength but the architecture can be easily generalized for wavelength division multiplexing (WDM). Our goal is to generate the N spatial and polarization components of the MVM signal as described by (1).

The transmitter design begins with a single semiconductor laser diode. Subsequently, a Mach-Zehnder modulator, followed by a phase modulator, can be employed to alter the pulse shape g(t), as well as the common amplitude A_m and phase ϕ_m of the MVM signal according to (1). After that, electro-optic splitters can be used to partition the signal into N parallel branches. By adjusting the control voltage of each Y-junction, an arbitrary power splitting ratio between its two output ports can be achieved. Recalling the hyper-spherical parametrization of the unit Jones vector $|s_m\rangle$ in (4), the power splitting ratio is $\cos^2(\phi_1):\sin^2(\phi_1)$ at the first Y-junction, $\cos^2(\phi_2):\sin^2(\phi_2)$

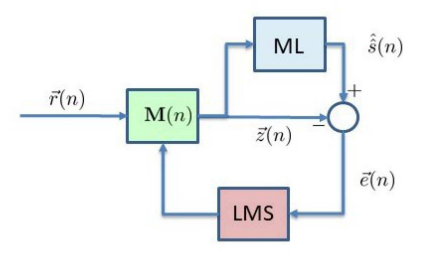


Fig. 5. Least mean squares (LMS) algorithm for polarization tracking [29].

at the second Y-junction, and so forth². Then, an array of phase modulators is used to generate phase differences among vector components. Finally, polarization controllers and polarization beam combiners are used to merge pairs of signals originating from different optical paths to create orthogonal states of polarization (SOPs) that are launched into separate fiber cores.

The purpose of the optical front-end and the DSP unit of the MVM receiver is to infer the Stokes components of the incoming spatial superchannel, which are given by (5), from a set of power measurements. To begin, it is necessary to separate the spatial and polarization components of the individual tributaries of the spatial superchannel using mode demultiplexers and polarization beam splitters. Then, an array of N photodiodes are used to measure their powers. In addition, polarization controllers and power splitters/couplers are used to combine the different spatial and polarization components pairwise in order to create N(N-1)/2 distinct combinations. The real and imaginary parts of the latter are measured using an array of 2N(N-1) identical photodiodes grouped in pairs. In total, $2N^2-N$ photodiodes are employed to measure all the elements of the dyad $\mathbf{S}=|s\rangle\langle s|$ independently [69].

However, by taking advantage of the interdependence of Stokes components, as they are functions of the 2N-2 hyperspherical coordinates of $|s\rangle$, it is possible to reduce the direct-detection receiver front-end complexity. In [69], we showed that O(N) photodiodes are sufficient to estimate the Stokes parameters of the spatial superchannel. Fig. 4(b) shows an example of a reduced-complexity direct-detection receiver for N=4.

For the purposes of this article, we assume that the simplifying assumptions of Section II-C hold, i.e., the optically-equalized communication channel exhibits negligible CD, MD, and MDL so that the residual transmission effects (random modal birefringence and random differential carrier phase shifts) can be modeled by a frequency-independent random unitary matrix. The action of this transfer matrix is a dynamic rotation of the received mode vector that varies slowly over time.

Stokes receiver DSP (Fig. 5) [29] can estimate Stokes vector rotations caused by fiber propagation and can counteract them by multiplying, in Stokes space, the received generalized Stokes vector $\vec{r}(n)$ at the n-th time instant with a compensating generalized $(N^2 - 1) \times (N^2 - 1)$ Müller matrix $\mathbf{M}(n)$. Alternatively, it is possible to perform optical derotation and MD/PMD

compensation of the received generalized Jones vector, which is driven by the Stokes vector receiver DSP.

Notice that the proper operation of MVM DD system does not require the absence of intermodal crosstalk. Intermodal crosstalk by itself can be mathematically represented as a generalized polarization rotation. The memoryless MIMO DSP equalizer in the MVM DD receiver can fully invert the channel transfer matrix in the generalized Stokes space and counteract intermodal crosstalk. In principle, there is virtually no signal-to-noise ratio penalty due to intermodal crosstalk.

The decisions of the Stokes vector receiver in Fig. 4(b) are based on the maximum a posteriori (MAP) criterion [9], which is equivalent to the maximum-likelihood criterion for equiprobable signals [9] (see Section IV-B). Applying the maximum-likelihood criterion in the generalized Jones space, we will show that the optimum decision maximizes the modulus of the inner product of Jones vectors (cf. (24)).

IV. SYMBOL ERROR PROBABILITY

In this Section, we describe the derivation of an upper bound for the back-to-back symbol error probability of the opticallypreamplified MVM DD receiver based on the union bound formalism [9].

A. Transmission Channel Model

We formulate the transmission channel by a discrete-time model [80]. All optical and electronic signals from now on are represented by their samples taken once per symbol.

After optical post-compensation, we assume that all transmission impairments are fully compensated. For instance, let \mathbf{U} denote the unitary Jones transfer matrix of the optical fiber due to modal birefringence. We assume that the unitary fiber transfer matrix \mathbf{U} is fully compensated, up to a random phase θ , by a zero-forcing optical adaptive equalizer with transfer matrix \mathbf{W} so that

$$\mathbf{W}\mathbf{U} = e^{i\theta} \mathbf{I}_N,\tag{9}$$

where I_N denotes the $N \times N$ identity Jones matrix.

After the optical front-end, at a given sampling instant, in the absence of noise, the incoherent receiver recovers the transmitted Jones vector $|s_m\rangle$ up to phase θ , which one could denote by $e^{i\theta}|s_m\rangle$.

Optical amplifiers introduce ASE noise, which is modelled as additive white Gaussian noise (AWGN). As a result, the received vector at a given sampling instant before photodetection equals [80]

$$|r\rangle = A_m e^{\iota \phi_m} e^{\iota \theta} |s_m\rangle + |n\rangle,$$
 (10)

where θ is uniformly distributed over $[0,2\pi)$ and $|n\rangle$ is a noise vector in Jones space. Notice that $|r\rangle$ and $|n\rangle$ are non-normalized Jones vectors, whereas $|s_m\rangle$ is a unit Jones vector.

Assuming identical optical amplifiers at the output of all cores, $|n\rangle$ has independent and identically distributed (i.i.d.) entries following a complex Gaussian distribution. The probability density

 $^{^2}$ An alternative design, similar to the one proposed by Kikuchi and Kawakami for SVM [79], would entail the use of a passive 1:N splitter, followed by an array of N parallel quadrature modulators, one at each individual transmitter branch.

function (pdf) of $|n\rangle$ is

$$\mathcal{P}(|n\rangle) = \frac{1}{(2\pi\sigma^2)^N} \exp\left(-\frac{\langle n|n\rangle}{2\sigma^2}\right),\tag{11}$$

where σ^2 denotes the noise variance per quadrature after the matched optical filter.

The noise energy in each spatial degree of freedom is

$$\mathcal{N}_0 = \frac{1}{2} \int_{-\infty}^{\infty} \mathbf{n}_{\nu}(t)^{\dagger} \mathbf{n}_{\nu}(t) dt = \sigma^2, \tag{12}$$

where $\mathbf{n}_{\nu}(t)$ is the complex noise component in a single quadrature plane of the electric field (given by any $|\nu\rangle \in \mathbb{C}^N$).

The symbol SNR γ_s , taking into account the noise over a spatial degree of freedom of the signal $|s_m\rangle$, is defined as

$$\gamma_s := \frac{\mathcal{E}_s}{\mathcal{N}_0} = \frac{A_m^2}{2\sigma^2} \mathcal{E}_g. \tag{13}$$

In the following, without any loss of generality, we assume that $A_m=1$ and $\mathcal{E}_g=1$, so

$$\gamma_s = \frac{1}{2\sigma^2}. (14)$$

The received dyad $\mathbf{R} = |r\rangle\langle r|$ is related to the transmitted dyad $\mathbf{S}_m = |s_m\rangle\langle s_m|$ by the *Stokes channel* formula:

$$\underbrace{|r\rangle\langle r|}_{\mathbf{R}} = \underbrace{|s_m\rangle\langle s_m|}_{\mathbf{S}_m} + \underbrace{2\Re\left(|s_m\rangle\langle n|\right) + |n\rangle\langle n|}_{\mathbf{N}_m},\tag{15}$$

where $\Re(.)$ denotes the real part. Observe that, in this formulation, the last two terms form a non-Gaussian noise \mathbf{N}_m exhibiting signal-noise and noise-noise beating

$$\mathbf{N}_m := 2\Re\left(|s_m\rangle\langle n|\right) + |n\rangle\langle n|. \tag{16}$$

As we indicated before, Jones vectors up to phase can be described by their dyads or their generalized real Stokes vectors in a higher-dimensional real vector space \mathbb{R}^{N^2-1} . Thus, the channel formula (15) could be expressed in three equivalent forms.

In translating to the generalized Stokes space, one has to keep in mind that the received Jones vector $|r\rangle$ is typically a non-unit vector (up to phase) and its dyad is expanded in the Gell-Mann basis as $\mathbf{R} = \frac{\langle r|r\rangle}{N}\mathbf{I}_N + \frac{1}{2C_N}\vec{r}\cdot\mathbf{\Lambda}$ (cf. (7)) so that the generalized Stokes vector $\vec{r}\in\mathbb{R}^{N^2-1}$ has squared norm $\|\vec{r}\|^2 = \langle r|r\rangle^2 = \operatorname{tr}(\mathbf{R}^2)$. The noise \mathbf{N}_m , which is a Hermitian matrix, could be Gell-Mann expanded in a similar way.

B. Optimum Decision Criterion for Equipower Signals

The decision scheme at the receiver uses the *maximum a* posteriori probability (MAP) criterion [9] to select a signal $\hat{s}_{\hat{m}}$ out of the set of M transmitted signals given that \vec{r} was received

$$\hat{m} := \underset{1 < m < M}{\operatorname{argmax}} \mathcal{P}(\hat{s}_m \mid \vec{r}). \tag{17}$$

From Bayes' theorem, the conditional probability distribution of \hat{s}_m given \vec{r} is

$$\mathcal{P}(\hat{s}_m \mid \vec{r}) = \frac{P_m \mathcal{P}(\vec{r} \mid \hat{s}_m)}{\mathcal{P}(\vec{r})},$$
(18)

where P_m is the probability of sending \hat{s}_m , $\mathcal{P}(\vec{r})$ is the marginal pdf of receiving \vec{r} , and $\mathcal{P}(\vec{r} | \hat{s}_m)$ is the likelihood pdf of receiving \vec{r} given that \hat{s}_m was sent.

By substituting (18) into (17) and omitting the common denominator $\mathcal{P}(\vec{r})$ (which does not influence the decision), we obtain

$$\hat{m} = \underset{1 < m < M}{\operatorname{argmax}} P_m \mathcal{P}(\vec{r} \mid \hat{s}_m). \tag{19}$$

In this article, we focus exclusively on equiprobable symbols, and, therefore, $P_m = 1/M$. In this case, the *maximum a posteriori probability* (MAP) criterion of (19) becomes equivalent to the *maximum-likelihood* (ML) criterion [9]

$$\hat{m} = \underset{1 \le m \le M}{\operatorname{argmax}} \, \mathcal{P}(\vec{r} \mid \hat{s}_m). \tag{20}$$

The likelihood pdf in (20) is obtained by considering the Jones vectors corresponding to \vec{r} and \hat{s}_m , noting that $|r\rangle - e^{\iota\theta}|s_m\rangle = |n\rangle$ by (10), and averaging the pdf (11) over all θ [9]:

$$\mathcal{P}(\vec{r} \mid \hat{s}_m)$$

$$= \frac{1}{(2\pi\sigma^2)^N} \int_0^{2\pi} \exp\left(-\frac{\||r\rangle - e^{i\theta}|s_m\rangle\|^2}{2\sigma^2}\right) \frac{d\theta}{2\pi}$$

$$= \frac{1}{(2\pi\sigma^2)^N} \exp\left(-\frac{\langle r|r\rangle - \langle s_m|s_m\rangle}{2\sigma^2}\right) I_0\left(\frac{|\langle r|s_m\rangle|}{\sigma^2}\right),$$
(21)

where we used the modified Bessel function of the first kind of zero order

$$I_0(x) := \frac{1}{\pi} \int_0^{\pi} \exp\left(x \cos \theta\right) d\theta. \tag{22}$$

Equality (21) is obtained by expanding in the exponent (cf. (15)):

$$|||r\rangle - e^{i\theta}|s_{m}\rangle||^{2}$$

$$= \langle r|r\rangle + \langle s_{m}|s_{m}\rangle - \underbrace{2\Re\left(e^{i(\theta - \theta_{m})}|\langle r|s_{m}\rangle|\right)}_{2\cos(\theta - \theta_{m})|\langle r|s_{m}\rangle|}, \quad (23)$$

where θ_m denotes the argument of $\langle r|s_m\rangle$ (which is immaterial). Based on (21), we can rewrite the maximum likelihood (ML) criterion (20) as [81]

$$\hat{m} = \underset{1 \le m \le M}{\operatorname{argmax}} |\langle r | s_m \rangle|, \tag{24}$$

where we used the monotonicity of $I_0(x)$ and the fact that $\langle s_m | s_m \rangle = 1$.

In particular, in the Jones space, the ML decision region $\mathcal{D}_m\subset\mathbb{C}^N$ for $|s_m\rangle$ is

$$\mathcal{D}_m = \{ |r\rangle : |\langle r|s_m \rangle| \ge |\langle r|s_{m'} \rangle| \text{ for all } m' \ne m \}.$$
 (25)

In passing, note that \mathcal{D}_m viewed in the Stokes space is the *Voronoi cell* around \hat{s}_m , and this is so irrespective of which applicable concept of distance, d_{ic} or d_{Stokes} , is used (cf. Section IV-D).

The symbol error probability is the expected probability of missing the right ML decision region, expressed by the following sum of integrals with respect to the 2N-dimensional volume in

 \mathbb{C}^N :

$$P_{\mathsf{e}|\mathsf{s}} = \sum_{m=1}^{M} P_m \sum_{m' \neq m} \int_{\mathcal{D}_{m'}} \mathcal{P}(\vec{r} \mid \hat{s}_m) \, d|r\rangle. \tag{26}$$

In principle, $P_{\rm e|s}$ can be computed based on the channel model, but its analytic evaluation is impossible for all but the simplest constellations due to the complex geometry of the ML decision regions \mathcal{D}_m . Therefore, readily computable analytic bounds on $P_{\rm e|s}$ are of value.

C. Union Bound

The general form of the union bound is [9]

$$P_{e|s} \le \sum_{m=1}^{M} P_m \sum_{m' \ne m} P_{e, \text{bin}}^{m'|m},$$
 (27)

where $P_{\mathrm{e,bin}}^{m'|m}$ is the pairwise error probability of deciding on $|s_{m'}\rangle$ when $|s_{m}\rangle$ was sent in a binary fashion, while no other symbols are considered. Therefore,

$$P_{\text{e,bin}}^{m'|m} = \int_{\mathcal{D}^{m'|m}} \mathcal{P}(\vec{r} \mid \hat{s}_m) \, d|r\rangle. \tag{28}$$

Above, the pairwise error decision region $\mathcal{D}^{m'|m}$ is where $P_{m'}\mathcal{P}(\vec{r}|\hat{s}_{m'}) \geq P_m\mathcal{P}(\vec{r}|\hat{s}_m)$, i.e., for equiprobable symbols,

$$\mathcal{D}^{m'|m} = \left\{ |r\rangle \in \mathbb{C}^N : |\langle r|s_{m'}\rangle| \ge |\langle r|s_m\rangle| \right\}. \tag{29}$$

Inequality (27) follows from the manifest inclusion $\mathcal{D}_{m'} \subset \mathcal{D}^{m'|m}$.

Our main result gives an explicit form for the terms in the union bound.

Theorem 1: The pairwise error probability between two equiprobable non-orthogonal unit vectors $|s_m\rangle, |s_{m'}\rangle \in \mathbb{C}^N$ is

$$P_{e,\text{bin}}^{m'|m} = Q_1 \left(\sqrt{\gamma_s} \rho_-, \sqrt{\gamma_s} \rho_+ \right) - \frac{1}{2} \exp\left(-\frac{\gamma_s}{2} \right) I_0 \left(\frac{\gamma_s \gamma}{2} \right), \tag{30}$$

where we defined the length parameters

$$\rho_{\mp}^2 := \frac{1 \mp \delta}{2},\tag{31a}$$

$$\delta := \sqrt{1 - \gamma^2},\tag{31b}$$

$$\gamma := |\langle s_m | s_{m'} \rangle| > 0, \tag{31c}$$

and Q_1 stands for the *Marcum Q-function* of the first order defined by [9]

$$Q_1(\mathbf{a}, \mathbf{b}) := \int_{\mathbf{b}}^{\infty} x \exp\left(-\frac{x^2 + \mathbf{a}^2}{2}\right) I_0(\mathbf{a}x) \, dx. \quad (32)$$

The formulas extend to the case of orthogonal signals, when $\gamma=0$ and one can fall back onto $Q_1(0,\mathbf{b})=\exp\left(-\frac{\mathbf{b}^2}{2}\right)$. To

improve readability, we leave the proof of Theorem 1 to Appendix A. For ease of reference, we instantiate (27) with (30) and record the following corollary.

Corollary 1: Given an MVM signal constellation represented by equiprobable unit Jones vectors $(|s_m\rangle)_{m=1}^M \in \mathbb{C}^N$ the symbol error probability $P_{\mathrm{e}|s}$ is bounded by

$$P_{e|s} \le \frac{1}{M} \sum_{m=1}^{M} \sum_{m' \ne m} \left[Q_1 \left(\sqrt{\gamma_s} \rho_-, \sqrt{\gamma_s} \rho_+ \right) - \frac{1}{2} \exp\left(-\frac{\gamma_s}{2} \right) I_0 \left(\frac{\gamma_s \gamma}{2} \right) \right]. \tag{33}$$

Below, we present asymptotic expressions that are valid for larger values of the symbol SNR γ_s and are obtained by implementing the results reported in [82] (proven in [83] and based on [84], [85]). The derivation of these formulas is given in Appendix B.

Corollary 2: For large values of the symbol SNR γ_s , when $\gamma_s \rho_+ \rho_- = \gamma_s \gamma/2$ is sufficiently large, we can use asymptotic expansions for $P_{e, \mathrm{bin}}^{m'|m}$, and the zeroth and first order approximations are as follows:

$$P_{\text{e,bin}}^{m'|m} \sim \frac{1}{2} \sqrt{\frac{\gamma}{1-\delta}} \operatorname{erfc}\left(\frac{\sqrt{\gamma_s}\sqrt{1-\gamma}}{\sqrt{2}}\right)$$

$$-\frac{1}{2\sqrt{\pi\gamma\gamma_s}} \exp\left[-\frac{\gamma_s(1-\gamma)}{2}\right] \qquad (34)$$

and

$$\frac{\partial_{e, \text{bin}}^{m'|m}}{\nabla \left[\frac{1}{2}\sqrt{\frac{\gamma}{1-\delta}} - \sqrt{\frac{1-\gamma}{\gamma}} \frac{1}{8\sqrt{2}} \left(\frac{1+\delta}{\gamma} + 3\right)\right]} \times \operatorname{erfc}\left(\frac{\sqrt{\gamma_s}\sqrt{1-\gamma}}{\sqrt{2}}\right) + \frac{1}{8\sqrt{\pi}} \left[\sqrt{2}\sqrt{\frac{1-\gamma}{1-\delta}} \left(\gamma\gamma_s\right)^{-\frac{1}{2}} - \left(\gamma\gamma_s\right)^{-\frac{3}{2}}\right] \times \exp\left[-\frac{\gamma_s(1-\gamma)}{2}\right]. \tag{35}$$

We note that the particular appeal of the asymptotic expressions in the corollary above is their ability to handle poorly separated vectors (with $\gamma \approx 1$). Pairs of vectors with small separation contribute the bulk of the $P_{\rm e|s}$. Moreover, MVM constellations with a given spectral efficiency per SDOF (e.g., analogous to QPSK) have diminishing minimal distance with the increase of the number of cores/modes.

When γ is not too close to 1 and the symbol SNR is large, we have a simpler asymptotic expression (with a straightforward

derivation given in Appendix B):

$$P_{\rm e,bin}^{m'|m} \sim \frac{1}{2} \frac{1}{\sqrt{\pi}} \sqrt{\frac{1+\gamma}{1-\gamma}} \frac{1}{\sqrt{\gamma}\sqrt{\gamma_s}} \exp\left[-\frac{\gamma_s(1-\gamma)}{2}\right].$$
 (36)

In any case, the leading exponential asymptotics is

$$\exp\left[-\frac{\gamma_s(1-\gamma)}{2}\right] = \exp\left[-\frac{1}{2}\gamma_s \frac{\mathsf{d}_{\mathrm{ic}}(\hat{s}_m, \hat{s}_{m'})^2}{2}\right], \quad (37)$$

where $\mathbf{d}_{\mathrm{ic}}(\hat{s}_m,\hat{s}_{m'})$ is the incoherent distance between \hat{s}_m and $\hat{s}_{m'}$ (as defined in Section IV-D, ahead). This indicates that the distance \mathbf{d}_{ic} is a natural way of expressing proximity of the symbols in our context.

We add that, if $\gamma=0$, (34)–(36) are not valid. However, then $P_{\rm e,bin}^{m'|m}$ equals $\frac{1}{2}\exp(-\gamma_s/2)$ and is eclipsed by the terms with $\gamma>0$ in the sum giving the union bound (27). Even though (34) and (35) work well even for moderately small values of γ , one can safely drop the terms with the smaller $\gamma\approx0$.

Appendices A and B are devoted to the proofs of the Theorem 1 and the Corollary 2, respectively. Section VII shows comparisons of the union bound for $P_{\rm e|s}$ obtained by using the above theoretical approximations and numerically-computed, Monte Carlo-based, values of $P_{\rm e|s}$ for several example constellations.

D. Distance Definitions

For the optimal geometric shaping of an MVM constellation, which is discussed in Section V, it is necessary to adopt some function of the distance between constellation points. The choice of a distance function depends on the detection scheme and the nature of the dominant channel impairments. For the back-to-back performance evaluation of optically-preamplified MVM DD receivers, we consider that ASE noise is the dominant impairment. In this case, for equienergetic MVM constellations, the suitable metric turns out to be the *chordal Fubini-Study distance*, which is a special case of what we call below *incoherent/DD distance*. We note that there are several arguments advocating naturality of this metric. Perhaps the strongest is based on the way it enters the previously derived asymptotic form of the union bound (37) for the symbol error probability.

One quick takeaway is that there is a better distance than the ordinary Euclidean Stokes distance, which is often the default choice and was also initially used in our computations (see Section V-B). Below, we define the *incoherent/DD distance* and relate it to other common distance functions.

1) Coherent Distance: In Jones space \mathbb{C}^N , we have the standard Euclidean distance between MVM symbols, which can be written as a function of the Hermitian inner product

$$d_{c}(|s\rangle, |s'\rangle) := |||s\rangle - |s'\rangle||$$

$$= \sqrt{\langle s|s\rangle - 2\Re\langle s|s'\rangle + \langle s'|s'\rangle}. \tag{38}$$

For unit vectors, (38) is expressed in terms of the *coherent angle* $\theta_c \in [0, \pi]$ as

$$d_{c}(|s\rangle,|s'\rangle) = \sqrt{2}\sqrt{1-\cos\theta_{c}}, \tag{39}$$

where $\cos \theta_c := \Re \langle s | s' \rangle$.

We refer to this distance as *coherent distance*, since the probability of making a binary error between $|s\rangle$ and $|s'\rangle$ in a coherent receiver depends on d_c in a natural way.

2) Incoherent Distance: In the case of incoherent detection, a transmitted MVM symbol is abstractly represented by a Jones vector up to phase, $e^{\iota\theta}|s\rangle$, with indeterminate $\theta\in[0,2\pi)$. Mathematically, as long as $|s\rangle\neq 0$, this is a circle in Jones space \mathbb{C}^N . From this standpoint, one might guess that the natural distance between symbols s and s' is the minimum coherent Jones distance between the two circles:

$$d_{ic}(|s\rangle,|s'\rangle) := \min_{\theta,\theta'} \|e^{\iota\theta}|s\rangle - e^{\iota\theta'}|s'\rangle\|$$

$$= \sqrt{\|s\|^2 - 2|\langle s|s'\rangle| + \|s'\|^2}. \tag{40}$$

When ||s|| = ||s'|| = 1, we can use the *incoherent/DD angle* $\theta_{ic} \in [0, \pi/2]$:

$$d_{ic}(|s\rangle, |s'\rangle) = \sqrt{2}\sqrt{1-\gamma},\tag{41}$$

where $\gamma := \cos \theta_{\rm ic} := |\langle s|s' \rangle|$.

In this case, the distance coincides with the *chordal Fubini-Study distance* on the complex projective space. In Appendices A and B, the incoherent cosine $\gamma = \cos\theta_{\rm ic} = |\langle s|s'\rangle|$ of two normalized symbols under consideration will make frequent appearance.

Of course, if only from $\Re\langle s|s'\rangle \leq |\langle s|s'\rangle|$, we have

$$d_{ic}(|s\rangle, |s'\rangle) \le d_{c}(|s\rangle, |s'\rangle)$$
 and $\theta_{ic} \le \theta_{c}$. (42)

The loss of phase information degrades one's ability to distinguish symbols.

3) Hilbert-Schmidt and Stokes Distance: Another way to represent incoherently-received symbols is with dyads $\mathbf{S} := |s\rangle\langle s|$. Their natural ambient linear space is $\mathrm{M}_{N\times N}(\mathbb{C})$ of all $N\times N$ complex matrices, which can be used together with the Hilbert-Schmidt Hermitian inner product $\mathrm{tr}(\mathbf{A}^{\dagger}\mathbf{B})$, where the operator $\mathrm{tr}(\cdot)$ denotes the trace of a matrix.

The *Hilbert-Schmidt distance* on $M_{N\times N}(\mathbb{C})$ is defined as

$$d_{HS}(\mathbf{A}, \mathbf{B}) := \|\mathbf{A} - \mathbf{B}\|_{HS}$$
$$= \sqrt{\operatorname{tr}(\mathbf{A}^{\dagger} \mathbf{A}) - 2 \Re \operatorname{tr}(\mathbf{A}^{\dagger} \mathbf{B}) + \operatorname{tr}(\mathbf{B}^{\dagger} \mathbf{B})}. \quad (43)$$

Restricted to dyads, since $\|\mathbf{S}\|_{HS}^2 = \langle s|s\rangle^2$ and $\operatorname{tr}(\mathbf{S}^\dagger\mathbf{S}') = |\langle s|s'\rangle|^2$ is already real, we get

$$d_{HS}(\mathbf{S}, \mathbf{S}') = \sqrt{\langle s|s\rangle^2 - 2|\langle s|s'\rangle|^2 + \langle s'|s'\rangle^2}.$$
 (44)

When $|||s\rangle||=|||s'\rangle||=1$, we could speak of $\it Hilbert\mbox{-}Schmidt$ angle and

$$d_{HS}(\mathbf{S}, \mathbf{S}') = \sqrt{2}\sqrt{1 - \gamma^2}, \text{ where } \gamma := |\langle s|s'\rangle|.$$
 (45)

Traditionally, incoherently-received MVM symbols are represented by Stokes vectors $\hat{s} \in \mathbb{R}^{N^2-1}$, whose entries are the coefficients of the expansion of the *trace-neutralized dyad* \mathbf{S} , e.g., $\mathbf{S} - \frac{1}{N}\mathbf{I}_N$ (assuming normalization $\langle s|s \rangle = 1$), with respect to the Gell-Mann matrix basis [73]. The Euclidean distance in Stokes space, called *Stokes distance*, coincides with the Hilbert-Schmidt distance up to scaling (having to do with the

said trace adjustment and the conventions for the Gell-Mann matrix basis):

$$d_{\text{Stokes}}(\hat{s}, \hat{s}') = 2C_N \sqrt{1 - \gamma^2}. \tag{46}$$

The Stokes distance is better suited for thermal noise-limited DD receivers, not for their ASE noise-limited counterparts, which have been the focus of this work.

V. GEOMETRIC CONSTELLATION SHAPING

A quintessential problem in digital communications systems is the optimal selection of signal sets to minimize the symbol error probability under various noise distributions and channel impairments. The term geometric constellation shaping means that the positions of constellation points in the signal space are selected appropriately in order to minimize the error probability. As a prototypical example, Foschini et al. [86] numerically optimized the shapes of two-dimensional signal constellations with arbitrary cardinality in the case of AWGN and coherent detection. Extending this work to optical communications, Karlsson and Agrell [87] investigated optimized power-efficient multidimensional modulation formats for coherent optical communications systems. For relatively small dimensions N, they used sphere-packing algorithms to optimize the constellation points. For larger dimensions, their design strategy was to select points from N-dimensional lattices [87].

In the case of SVM (N = 2), geometric constellation shaping for equipower signal sets (PolSK) was performed numerically, initially by Betti et al. [22], by maximizing the minimum Euclidean distance among signals in Stokes space, and then, by Benedetto and Poggiolini [25], by using the exact symbol error probability of M-ary PolSK as an objective function. To derive a formula for the symbol error probability, Benedetto and Poggiolini calculated the boundaries of the decision regions, initially considering signal vectors in Stokes space that were placed at the vertices of a regular polyhedron inscribed within the Poincaré sphere, and then extending the analysis to generic equipower constellations with constellation points at the vertices of irregular polyhedra [25]. Optimum signal constellations for the case of N=2 and M=4, 8, 16 and 32 signals were derived [25]. Kikuchi [27] used suboptimal 2D quaternary and cubic octary constellations for implementation simplicity. Morsy-Osman et al. [40] designed intensity/polarization SVM constellations based on the face-centered cubic (FCC) lattice to achieve maximum packing density, assuming a thermal-noiselimited scenario and using the minimum Euclidean distance criterion.

Our goal here is to spread out the MVM constellation points on the surface of the Poincaré sphere in the generalized Stokes space and, thus, improve the symbol error probability in a DD based link. Since the adoption of symbol error probability as objective function leads to a computationally-intensive numerical optimization, a suitably-selected simplified objective function is used instead. The gradient-descent method [88] is used for the minimization of the simplified objective function.

To facilitate calculations, we consider an objective function from electrostatics [89], wherein the constellation points are assumed to be identical charges on the surface of a perfectly-conducting Poincaré hypersphere. Starting from given initial positions, the charges are allowed to equilibriate under the action of Coulomb forces. In other words, we recast the original three-dimensional Thomson problem [89] to higher-dimensional Stokes space. This adaptation requires constraining the M constellation points to a (2N-2)-dimensional manifold due to the relationships (4), (5) relating the higher-dimensional Jones and Stokes spaces [72], [73], [74]. The manifold is equivalent to the complex projective space.

It is worth saying a few words here about the extensive literature on the Thomson problem. Since the original publication of the problem by J. J. Thomson in 1904, numerous papers were written on this topic and its variants. Saff and Kuijlaars [90] give a comprehensive survey of the literature in the two dimensional case N=2, with an emphasis on the case when M is large. Global minima for the Thomson Problem for N=2 are posted on the Cambridge website [91].

The function SpherePoints[n] in Wolfram *Mathematica* [92] gives the positions of n approximately uniformly distributed points on the surface of the S^2 unit sphere in three dimensions, with exact values for certain small n and a spiral-based approximation for large n [92].

Closely related to Thomson's problem is the Tammes problem whose goal is to find the arrangement of M points on a unit sphere which maximizes the minimum Euclidean distance between any two points. Jasper et al. [93] studied the Tammes problem in the complex projective space and maintain a website listing the current best-known numerical approximations [94].

A. Gradient Computation

Consider a perfectly-conducting Poincaré hypersphere with identical charges at the positions of the constellation points, which are constrained to the complex projective space manifold. As charges repel each other with Coulomb forces, they move within the manifold until they reach an equilibrium distribution with minimum potential energy.

The electrostatic potential energy $\Omega(d_{ij})$ of two charges i,j separated by a distance d_{ij} is inversely proportional to their distance: $\Omega(d_{ij}) \sim d_{ij}^{-1}$. The total electrostatic potential energy U of a system of M charges can be obtained by calculating the potential energy $\Omega(d_{ij})$ for each individual pair of charges i,j and adding the potential energies for all distinct combinations of charge pairs

$$U = \sum_{i=1}^{M} \sum_{j=i+1}^{M} \Omega(d_{ij}). \tag{47}$$

The distances d_{ij} can be calculated in terms of the corresponding unit Jones vectors $|s_i\rangle \in \mathbb{C}^N$, $i=1,\ldots,M$, as follows:

$$d_{ij} = \psi\left(|\langle s_i | s_j \rangle|^2\right) = \psi\left(\gamma^2\right). \tag{48}$$

We leave the function ψ unspecified for now to allow use of various distances between vectors (cf. Section IV-D).

To compute the gradient, we first assume that the Jones vectors depend on a certain parameter t and compute

$$\frac{\partial U}{\partial t} = \sum_{i < j} \Omega'(d_{ij}) \frac{\partial d_{ij}}{\partial t}$$

$$= \sum_{i < j} \Omega'(d_{ij}) \psi' \left(|\langle s_i | s_j \rangle|^2 \right) \frac{\partial |\langle s_i | s_j \rangle|^2}{\partial t}$$

$$= \sum_{i < j} \Omega'(d_{ij}) \psi' \left(|\langle s_i | s_j \rangle|^2 \right)$$

$$\cdot 2\Re \left(\langle s_j | s_i \rangle \left\langle \frac{\partial s_i}{\partial t} \middle| s_j \right\rangle + \langle s_i | s_j \rangle \left\langle \frac{\partial s_j}{\partial t} \middle| s_i \right\rangle \right), \tag{49}$$

where primes denote derivatives and we used multilinearity to evaluate $\frac{\partial |\langle s_i | s_j \rangle|^2}{\partial t}$.

Taking t to be the real and imaginary parts of $s_{im} = x_{im} +$ ιy_{im} , the components of the gradient of U are found as

$$\frac{\partial U}{\partial x_{im}} = \sum_{i: j \neq i} \Omega'(d_{ij}) \psi'\left(|\langle s_i | s_j \rangle|^2\right) 2\Re\left(\langle s_j | s_i \rangle s_{jm}\right) \quad (50)$$

$$\frac{\partial U}{\partial y_{im}} = \sum_{j: j \neq i} \Omega'(d_{ij}) \psi'\left(|\langle s_i | s_j \rangle|^2\right) 2\Im\left(\langle s_j | s_i \rangle s_{jm}\right), \quad (51)$$

where $\Im(.)$ denotes the imaginary part. To state the end result, the gradient³ ∇U is the vector of real and imaginary parts of the (complex) vector $\left(\frac{\partial U}{\partial s_{im}}\right) \in \mathbb{C}^{M \times N}$ given by

$$\frac{\partial U}{\partial s_{im}} = 2 \sum_{j: j \neq i} \Omega'(d_{ij}) \psi'\left(|\langle s_i | s_j \rangle|^2\right) \langle s_j | s_i \rangle s_{jm}. \tag{52}$$

B. Example: Coulomb Potential

In the following, we adapt the three-dimensional Thomson problem [89] to the generalized Stokes space. It is true that the use of the electrostatic potential energy as an objective function in lieu of the symbol error probability is not justified by the underlying physics of the problem under study. Nevertheless, as shown in Fig. 15, the minimization of the electrostatic potential yields nearly optimal results that are very close to the ones obtained by minimizing the symbol error probability.

For the Thomson problem, we use the Euclidean distance d_{Stokes} in the Stokes space, per (46), so that (48) is written as

$$\psi(t) := 2C_N \sqrt{1 - t},\tag{53}$$

where now
$$t=\gamma^2$$
. From $\psi(t)^2=-4C_N^2t+{\rm Const},$ we get $\psi'(t)=-2C_N^2\psi(t)^{-1},$ so

$$\frac{\partial U}{\partial s_{im}} = -4C_N^2 \sum_{j: j \neq i} \Omega'(d_{ij}) \psi \left(|\langle s_i | s_j \rangle|^2 \right)^{-1} \langle s_j | s_i \rangle s_{jm}$$

 3 N.B.: This is not a complex derivative as U is not necessarily analytic.

$$= -4C_N^2 \sum_{j: j \neq i} \Omega'(d_{ij}) d_{ij}^{-1} \langle s_j | s_i \rangle s_{jm}.$$
 (54)

Furthermore, for the case of electrostatic Coulomb forces acting in the Stokes space, we have the inverse distance potential

$$\Omega(d_{ij}) = d_{ij}^{-1}, \quad \Omega'(d_{ij}) = -d_{ij}^{-2}.$$
 (55)

Thus, instantiating (52) yields

$$\frac{\partial U}{\partial s_{im}} = 4C_N^2 \sum_{j: j \neq i} d_{ij}^{-3} \langle s_j | s_i \rangle s_{jm}.$$
 (56)

C. Numerical Details

We developed an efficient, partially-compiled Mathematica code implementing the gradient-descent optimization algorithm for arbitrary potential energies. This implementation is adequately fast on a personal computer to enable design of MVM constellations with up to M=1024 points for up to N=8spatial degrees of freedom (SDOFs) (see Fig. 18).

The gradient-descent optimization algorithm starts with either a randomly-generated constellation or a small random perturbation of a deterministic constellation. To give an example, consider the following deterministic constellation of Jones vectors: their first component is set equal to unity, while their remaining N-1 components take all possible combinations of values in $\{\pm 1, \pm \iota\}$. Finally, the Jones vector length is normalized to unity. This process yields an MVM constellation with $M=4^{N-1}$ vectors. We call it the standard constellation. Mathematically, it represents the orbits of the vertices of a hypercube in \mathbb{C}^N under the circle action by the phase rotation. For this reason, its more descriptive name could be standard reduced hypercube constellation or standard reduced Jones hypercube constellation.

VI. BIT-TO-SYMBOL MAPPING

Once we have geometrically optimized a constellation $(|s_m\rangle)_{m=1}^M$ to reduce the symbol errors, we seek to minimize bit errors by optimizing the bit-to-symbol mapping. In commonlyused modulation formats, such as M-PAM, M-PSK, M-QAM on a square lattice, and their generalization to cubic lattices of any dimension, this task is achieved via *Gray coding* [95]. Unfortunately, in general, no such labeling readily exists for the MVM format.

Given a bit encoding $(\mathbf{b}_m)_{m=1}^M$, where the length of each bit block \mathbf{b}_m is $k = \log_2(M)$, we use the union bound (27) to find that the average bit error probability $P_{e|b}$ (at a symbol SNR γ_s) is bounded by

$$P_{e|b} \le \frac{1}{kM} \sum_{m=1}^{M} \sum_{m' \ne m} P_{e,\text{bin}}^{m'|m} h_{mm'},$$
 (57)

where $h_{mm'}$ denotes the *Hamming distance* between \mathbf{b}_m and $\mathbf{b}_{m'}$. This is based on the observation that the expected number of bit errors corresponding to mistakenly receiving $|s_{m'}\rangle$ when $|s_m\rangle$ was transmitted is $P_{\mathrm{e,bin}}^{m'|m}h_{mm'}$. We use the right side of (57) as an objective function ξ for evaluating various bit encodings:

$$\xi = \xi \left((|s_m|)_{m=1}^M, (\mathbf{b}_m)_{m=1}^M, \sigma^2 \right)$$

$$= \frac{1}{kM} \sum_{m=1}^M \sum_{m' \neq m} P_{\text{e,bin}}^{m'|m} h_{mm'}. \tag{58}$$

Finding a bit encoding $(\mathbf{b}_m)_{m=1}^M$ that minimizes ξ at a symbol SNR γ_s serves as a proxy for minimizing bit errors for a given constellation and, thus, finding the optimal bit-to-symbol mapping. With M! possible encodings, the sheer number of combinations prohibits brute-force solutions for all but the smallest constellations. This optimization problem can be viewed as a type of $Quadratic\ Assignment\ Problem\ [96]$, i.e., the optimal assignment of $\{1,2,\ldots,M\}$ (in binary) to $(|s_m\rangle)_{m=1}^M$ with pairwise distances given by $\frac{1}{kM}P_{\mathrm{e,bin}}^{m'|m}$ and pairwise weights given by Hamming distances $h_{mm'}$. Quadratic Assignment Problems are known to be NP-hard [97] and encompass the classical $Traveling\ Salesman\ Problem$ as a special case.

Given these rapidly scaling combinatorics, we turn to numerical minimization. In particular, *simulated annealing* has a long history of use for combinatorial optimization problems [98] and lies within the broader class of *Metropolis-Hastings algorithms*. Inspired by metallurgy, simulated annealing algorithms work by stochastically exploring the search space, helping prevent the algorithm from becoming entrapped near local minima.

Our implementation begins with an initial bit-to-symbol mapping $(\mathbf{b}_m)_{m=1}^M$ (either randomly selected or the current best known encoding) and a sequence of temperatures (T_n) per a selected cooling schedule [98]. In each iteration, a new candidate encoding $(\mathbf{b}'_m)_{m=1}^M$ is generated by randomly swapping the bit encodings for two symbols. We then compare $\xi((\mathbf{b}'_m)_{m=1}^M)$ against $\xi((\mathbf{b}_m)_{m=1}^M)$. If $\xi((\mathbf{b}'_m)_{m=1}^M) < \xi((\mathbf{b}_m)_{m=1}^M)$, then $(\mathbf{b}'_m)_{m=1}^M$ is automatically accepted. Otherwise, $(\mathbf{b}'_m)_{m=1}^M$ is probabilistically accepted or rejected by comparing $\exp\{[\xi((\mathbf{b}_m)_{m=1}^M) - \xi((\mathbf{b}'_m)_{m=1}^M)]/T_n\}$ against a uniformly randomly generated value in [0,1]. The initial high temperatures give a higher probability of accepting a candidate encoding $(\mathbf{b}'_m)_{m=1}^M$ in order to explore the search space, while the final low temperatures exploit local optimizations.

Implementing a simulated annealing optimization algorithm inherently requires significant tuning of parameters. Choices such as initial and final temperatures, cooling schedule, and number of iterations must all be carefully selected for the specific problem in order to properly balance exploration versus exploitation. After an investigation of various cooling schedules, we established that a classic exponential cooling schedule of $T_n = \alpha^n T_0$, where α denotes the cooling factor, was well-suited to this problem. With further experimentation, we found that setting the initial temperature T_0 as the standard deviation of ξ for a random sample of bit encodings gave acceptable performance across a wide range of constellation sizes M, without the need for extensively tuning this parameter.

We remark that the constellation $(|s_m\rangle)_{m=1}^M$ is static and the $P_{\mathrm{e,bin}}^{m'|m}$ terms in (58) are computed once at the outset and then stored for all future evaluations of ξ .

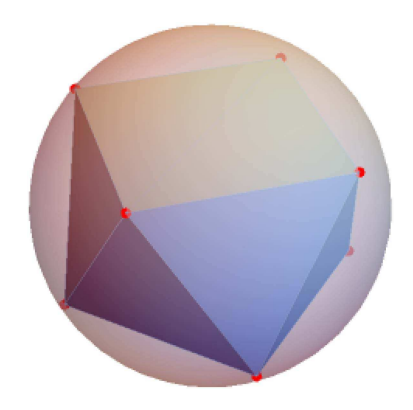


Fig. 6. Square antiprism (Conditions: N = 2, M = 8).

Finally, we note that $h_{mm'}$ is trivially bounded by k for all $m \neq m'$. Hence the performance increase that can possibly be achieved by optimizing the bit-to-symbol mapping $(\mathbf{b}_m)_{m=1}^M$ is limited by a factor of k (cf. Fig. 14), in contrast to the several orders of magnitude of performance improvement that can be obtained by geometrically optimizing the constellation $(|s_m\rangle)_{m=1}^M$ (cf. Fig. 15). Therefore, the allocation of computation time when generating an (N,M)-MVM format should place greater emphasis on geometric optimization, while not completely neglecting to optimize the bit-to-symbol mapping.

VII. RESULTS AND DISCUSSION

In Sections IV and V, we derived an upper bound for the symbol error probability of (N,M)-MVM and discussed accelerated geometric constellation shaping in the generalized Stokes space using an electrostatic analog (i.e., an extension of the Thomson problem to higher dimensions). In Section VI, we proposed a method to optimize the bit-to-symbol mapping of arbitrary MVM constellations using simulated annealing. In this section, we navigate the reader through the steps of the formalism presented in Sections IV–VI by providing illustrative examples for specific N,M.

A. Constellation Design

As a starting point, to develop some physical intuition by visualization, we consider constellation shaping and bit-to-symbol mapping in the three-dimensional Stokes space.

We first examine the optimal distribution of eight points on the surface of the Poincaré sphere S^2 . From [25], we know that the optimal constellation corresponds to a square antiprism inscribed in the sphere as shown in Fig. 6 (rather than a cube as proposed by [27]). We want to test whether the solution of the Thomson problem using the method of gradient descent coincides with the solution of [25].

Fig. 7 shows the evolution of the potential energy given by (47) as a function of the number of gradient descent iterations associated with 100 different random initial configurations of M=8 point charges on S^2 . After about 1,000 iterations, all cases converge to essentially identical square antiprisms (up to arbitrary 3D rotations), like the one shown in Fig. 6.

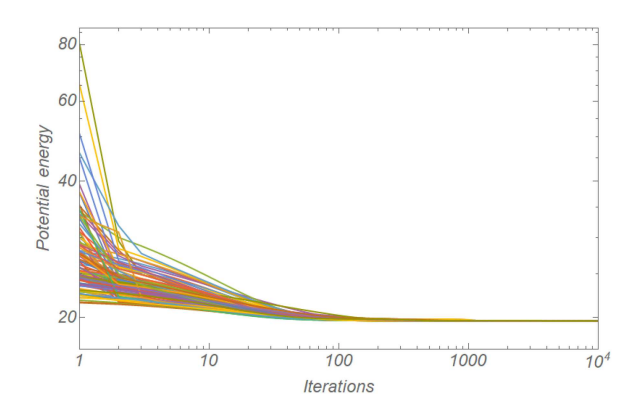


Fig. 7. Thomson algorithm convergence for 100 distinct initial configurations (Conditions: $N=2,\ M=8$). After roughly 1000 iterations, all cases have converged to square antiprisms.

000 1,29 100 001 1,17 1,17 1,17

Fig. 8. Bit-to-symbol mapping for the square antiprism (Conditions: N=2, M=8). The red, green, and black edges have lengths of approximately 1.17, 1.17, and 1.29, respectively.

Close inspection reveals that the Euclidean distances between constellation points provided by the solution of the Thomson problem using the method of gradient descent in Fig. 7 are slightly different from the ones provided by [25]. Actually, the constellation of [25] is unstable from an electrostatic point-of-view. In other words, if the constellation of [25] is provided as an initial configuration for the Thomson problem, the gradient in (56) of the potential energy in (47) is non-zero, and, therefore, the constellation points experience Coulomb forces that move them to slightly different final positions. The same holds if one uses as initial guesses for the Thomson problem various point configurations provided by the minimization of alternative cost functions, e.g., for the Tammes problem [93].

In conclusion, the polytopes provided by the minimization of different cost functions for N=2, M=8 correspond to slightly different square antiprisms. For practical engineering purposes, however, we consider that these differences among various constellation configurations are immaterial and that the numerical solution of the Thomson problem using the method of gradient descent provides sufficient optimization effectiveness at low computational cost.

Next, we shift our focus to the optimal bit-to-symbol mapping for the square antiprism. To facilitate visualization, we represent the configuration of the constellation points on the surface of the Poincaré sphere by a two-dimensional graph whose vertices represent the constellation points and whose edges represent closest neighbors. For the case of the square antiprism of Fig. 6, we obtain the graph shown in Fig. 8. The two square faces on the opposite sides of the square antiprism are shown in red and green respectively, and the edges interconnecting them are shown with dotted black lines. The two square faces have sides equal to 1.17 and the edges interconnecting them are 1.29 long.

In Gray coding, the closest neighbors at distance 1.17 are assigned binary words that differ in only one bit, i.e., they have a Hamming distance of one. Since each vertex in Fig. 8 has only two closest neighbors belonging to the same square face, it is straightforward to Gray label the vertices of the square faces using all binary words of three bits. For instance, one can Gray code the green square using the binary words with their most significant bit (msb) equal to zero and then use the remaining

binary words with their msb equal to one for the red square. The proposed bit-to-symbol mapping in Fig. 8 is just one of many possible Gray mappings.

However, since the second-closest neighbors at distance 1.29 are not very different distance-wise compared to the first neighbors at distance 1.17, we have to take into account that erroneous symbol decisions can lead to second-closest neighbors with significant probability. The proposed bit-to-symbol mapping in Fig. 8 offers almost all the benefits of Gray coding. Each symbol error leads to 3 neighboring nodes that differ by one bit and to only one neighboring node that differs by two bits.

In this particular case, the problem of assigning binary words to constellation points in order to minimize the bit error probability can be solved manually as follows: starting with the green square, we go in the clockwise direction and assign bits to symbols using all Gray words of zero msb. Then, starting from the vertex between 000 and 001, we trace the red square in the counterclockwise direction and assign bits to symbols using all Gray words of unit msb. We verified that the solution obtained via the simulated annealing algorithm is indeed the one found manually in Fig. 8. This is evidence that the simulated annealing algorithm performs adequately.

In order to further validate bit-to-symbol mappings provided by our simulated annealing algorithm, we ran benchmarking tests on constellations that admit Gray coding [99] (e.g., *M*-PSK and *M*-QAM). Our implementation of the simulated annealing algorithm displayed strong performance in these tests, often finding the global minimum for small constellation sizes.

For larger M, the computational complexity of assigning binary words to constellation points in order to minimize the bit error probability grows exponentially. Let us see why that is: There are M! ways that we can assign M words of k bits to the M nodes. Using the dominant term in Stirling's approximation for factorials, we see that $M! \sim M^M e^{-M}$ for $M \gg 1$. Computing the objective function for all possible arrangements and selecting the bit-to-symbol mapping that yields the global minimum is clearly computationally prohibitive for large values of M. Simulated annealing can be used to solve such combinatorial optimization problems. While it may not find globally optimal solutions, evidence from tests performed

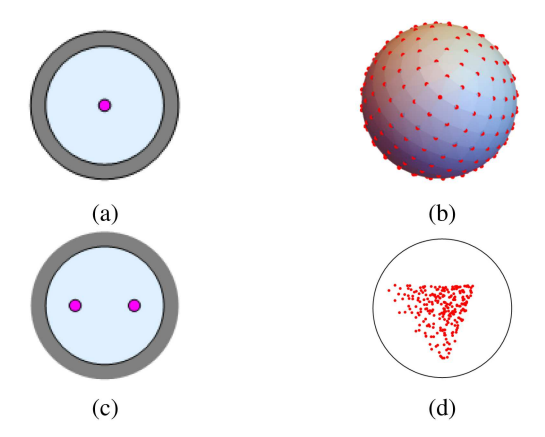


Fig. 9. Illustration of optimized constellations (b), (d), with M=256 points for (a) SMF (N=2); and (c) dual-core MCF (N=4), respectively.

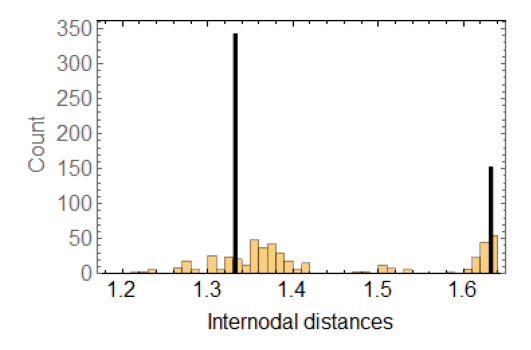


Fig. 10. Histograms of internodal distances. (Yellow: Thomson problem; Black: Tammes problem [93]). (Conditions: $N=4,\,M=32$).

on small constellation sizes suggests that simulated annealing can produce bit-to-symbol mappings that are sufficiently nearly-optimal.

We continue by examining constellation shaping and bit-tosymbol mapping in higher-dimensional Stokes spaces based on the physical intuition provided by the three-dimensional Stokes space.

Examples of optimized constellations for N=2 and N=4 and M=256 are shown in Fig. 9(b), (d), respectively.

To illustrate the difficulties of bit-to-symbol mapping in higher-dimensional Stokes spaces, let us take a closer look at the optimized MVM constellation for $N=4,\ M=32.$ The histograms of internodal distances for the Thomson problem and the Tammes problem [94] are shown in Fig. 10. Notice that the constellations found by solving these two problems are not identical. For instance, there are 343 closest neighbor pairs at distance 1.33 in the Tammes problem, whereas the Thomson problem gives a continuum-like distribution of internodal distances in the range 1.1-1.6 for the closest neighbors. Choosing the Tammes problem solution due to its high degree of symmetry, we make a 2D graph of the 32 vertices with edges interconnecting closest neighbors only (Fig. 11). Since the average vertex degree in the graph is 21 (Fig. 12), it is obvious that Gray coding cannot be applied. For 32 constellation points, the number of possible codings is $32! \approx 2.6 \times 10^{35}$, so a brute force optimization by exhaustive enumeration is impossible. A

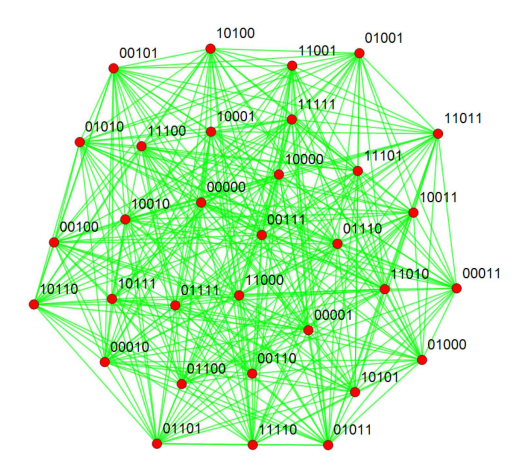


Fig. 11. Constellation graph and bit-to-symbol mapping (Conditions: ${\cal N}=4, M=32$).

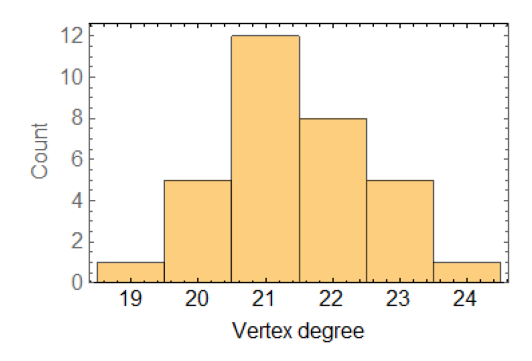


Fig. 12. Histogram of vertex degrees for the constellation graph of Fig. 11 (Conditions: $N=4,\,M=32$).

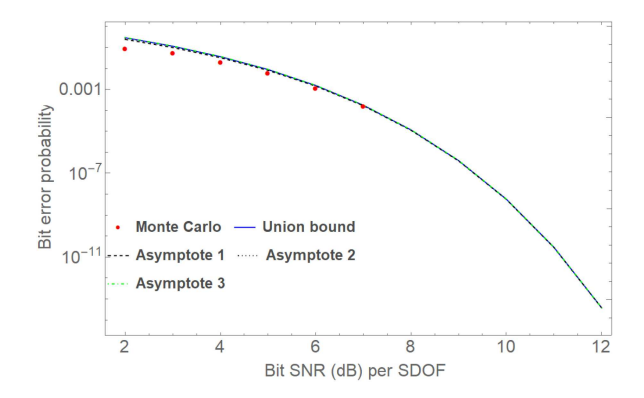


Fig. 13. Bit error probability vs bit SNR (dB) per SDOF (Points: Monte Carlo simulation; Blue line: union bound (Corollary 1); dashed lines: asymptotics (Corollary 2). (Conditions: N=8, M=64).

bit-to-symbol mapping given by simulated annealing is shown in Fig. 11.

B. Validity of the Error Probability Upper Bounds

The symbol error probability for equienergetic signals is bounded by using the analytical union bound of Corollary 1. We want to gain insight into the validity and the tightness of this bound at various bit SNRs. In Fig. 13, we check the validity of Corollary 1 and the asymptotic expressions of Corollary 2 by Monte Carlo simulation. We observe that the union bound is

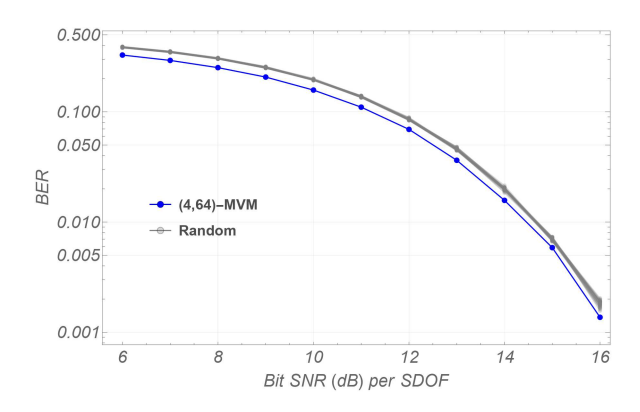


Fig. 14. Bit error rate (BER) versus bit SNR per SDOF for the optimized bit-to-symbol mapping (in blue) and randomized bit-to-symbol mappings (in gray).

asymptotically tight and spot-on for bit error probabilities below the order of 10^{-3} . Otherwise, the union bound overestimates larger error probabilities due to the significant overlap between the pairwise decision regions.

C. Impact of Bit-to-Symbol Mapping

Fig. 14 compares the bit error rates (computed using Monte Carlo simulation) of the optimized bit-to-symbol mapping provided by simulated annealing (in blue) against multiple randomized encodings (in gray) for the same (4,64)-MVM constellation. We observe a performance gain of the optimized encoding over randomized encodings across a wide range of bit SNRs. In particular, we note that our bit-to-symbol mapping optimization requires a concrete choice of noise level σ^2 in defining the objective function of (58) for simulated annealing. Hence it is possible that the suitability of an encoding might change with the noise level, requiring different optimizations for different noise levels. However, Fig. 14 shows that a bit-to-symbol mapping optimized at one noise level (in this case, a bit SNR per SDOF of 10 dB) performs well across a range of SNRs, showing that this concern is immaterial in practice.

D. Potential Selection for Constellation Optimization

We use the union bound of Corollary 1 to compare the performance of various (4,64)-MVM constellations obtained via different optimization methods. Fig. 15 shows the symbol error probability $P_{\rm e|s}$ as a function of the symbol SNR per SDOF. The blue and orange curves correspond to constellations obtained using the gradient descent method with a Thomson (Coulomb) potential and with the union bound based on Corollary 1 as an objective function, respectively. The green curve is a numerical approximation of a solution to the Tammes problem using the Matlab code provided by [93]. Finally, as a baseline for our analysis, the red curve corresponds to a standard Jones hypercube constellation (cf. Section V-C).

Given the different algorithmic approaches and computational complexities of these methods, the parameters are selected in such a way that each implementation takes roughly the same amount of computing time in order to provide a fair comparison. Using the union bound as the objective function yields the best

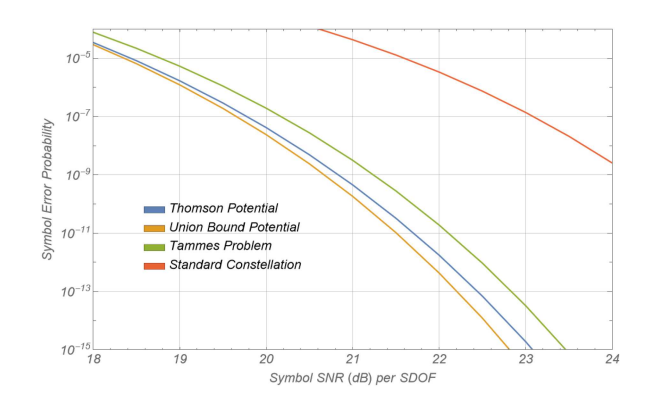


Fig. 15. Performance comparison of different (4,64)-MVM constellations optimized using various potential functions and algorithms.

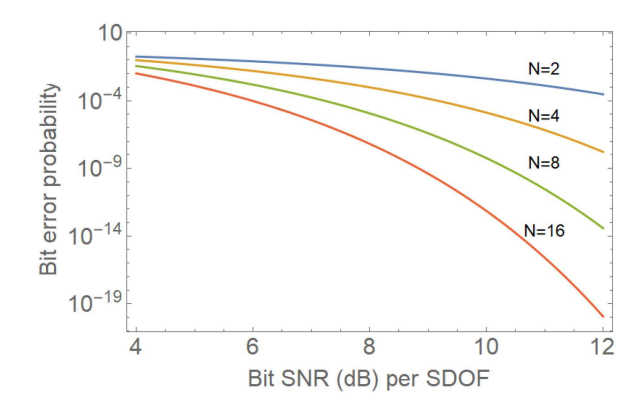


Fig. 16. Bit error probability of $M-{\rm ary}$ MVM based on SIC-POVM vectors vs the bit SNR per SDOF.

performing constellation, as befits its intrinsic nature, despite its high computational complexity resulting in fewer gradient descent steps in the allotted time. Belying its extrinsic motivation, the Thomson method performs remarkably well, with only a slightest penalty compared to the Union Bound potential. The Tammes Problem method also performs quite well, with only a marginal performance loss compared to the Union Bound method. Finally, we observe that all three numerical optimizations outperform the standard Jones hypercube constellation by more than 3 dB at low symbol error probabilities.

E. Simplex MVM Constellations

In Fig. 16, we plot the upper limit of the bit error probability of simplex MVM constellations, given by SIC-POVM vectors, for an optically-preamplified MVM DD receiver with a matched optical filter, as a function of the bit SNR per SDOF. The Jones space dimension varies from N=2 to N=16 in power-of-two increments for different lines from top to bottom. The accuracy of the curves has also been checked by Monte Carlo simulation and the numerical data agree asymptotically with the analytical curves, however, the Monte Carlo simulation results have been omitted from Fig. 16 to avoid clutter. We observe that the bit SNR required to achieve a given bit error probability decreases as N increases. This is explained by the squared incoherent distance between two SIC-POVM Stokes vectors equaling $\mathbf{d}_{ic}^2=2(1-1/\sqrt{N}+1)$, which is an increasing function of N. (In

contrast, the squared Stokes distance $d_{Stokes}^2 = 2(1+1/(N^2-1))$ decreases, highlighting the superiority of d_{ic} over d_{Stokes} in this context.)

F. Performance Comparison of Various Modulation Formats

Armed with Corollary 1, we want to compare the performance of MVM with that of conventional modulation formats for shorthaul transmission and optically-preamplified direct detection.

For a fair comparison, we want to select the MVM constellation cardinality so that MVM exhibits the same spectral efficiency as conventional modulation formats. In single-mode transmission, spectral efficiency is defined as the ratio of the net bit rate after FEC to the channel bandwidth. Here, we use the following definition of the spectral efficiency per SDOF: Let the symbol interval be T_s and the symbol rate be $R_s = T_s^{-1}$. Assuming ideal Nyquist pulses and since MVM is a carrier modulation, the signal bandwidth B_s is equal to the symbol rate R_s . Suppose that the bit interval is T_b and the bit rate is R_b . Let M be the number of constellation symbols. Then, $k = \log_2 M$ bits are transmitted per symbol interval. We define the spectral efficiency per SDOF as $\eta := R_b/(NB_s)$. Since $T_s = kT_b$ and $R_b = kR_s$, the spectral efficiency per SDOF is $\eta = kN^{-1}$.

For instance, for SIC-POVMs, there are $M=N^2$ constellation points and, therefore, the spectral efficiency per SDOF is $\eta=2\,N^{-1}\log_2\,N$. Consequently, by increasing the dimensionality N of Jones space, the normalized spectral efficiency per SDOF decreases.

For illustration, suppose we have an ideal homogeneous MCF with eight identical single-mode cores. The most straightforward way to use this fiber is to transmit 8 independent parallel channels, each carrying a binary signal, e.g., based on either intensity modulation (IM), binary DPSK (DBPSK), or binary SVM (BSVM). When ideal Nyquist pulses with zero roll-off factor are used, all the aforementioned modulation formats can achieve a theoretical spectral efficiency of 0.5 b/s/Hz/SDOF.

Alternatively, rather than using the 8 cores independently, we can transmit a single MVM channel by sending pulses over all eight cores in parallel, i.e., simultaneously utilizing all 16 available SDOFs. Therefore, we should choose (16,256)-MVM, which results in a spectral efficiency 0.5 b/s/Hz/SDOF as well. In the 255-dimensional generalized Stokes space, the optimal (16,256)-MVM constellation corresponds to a 256-simplex [66].

In Fig. 17, we present analytical plots of the bit error probability vs. the bit SNR per SDOF at the decision device. Single-polarization, optically-preamplified, direct-detection receivers require 15.83 dB, 13 dB, and 16 dB for IM [100], DBPSK [100], and BSVM [44], respectively, to achieve a bit error probability of 10^{-9} . In contrast, the (16, 256)-MVM optically-preamplified, direct-detection receiver requires only 8.84 dB, to achieve the same bit error probability. This corresponds to bit SNR gains of 4.16 dB, 7 dB, and 7.16 dB over DBPSK, IM, and BSVM, respectively. We conclude that the use of MVM can greatly improve system performance over conventional modulation formats at the expense of transceiver complexity [66].

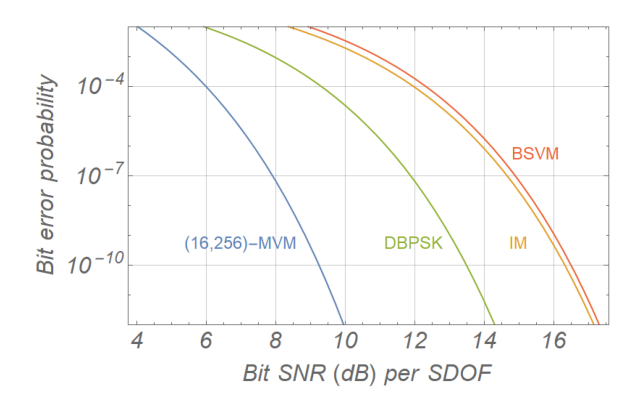


Fig. 17. Bit error probability for (16,256)-MVM in comparison to conventional modulation formats for an 8-core MCF.

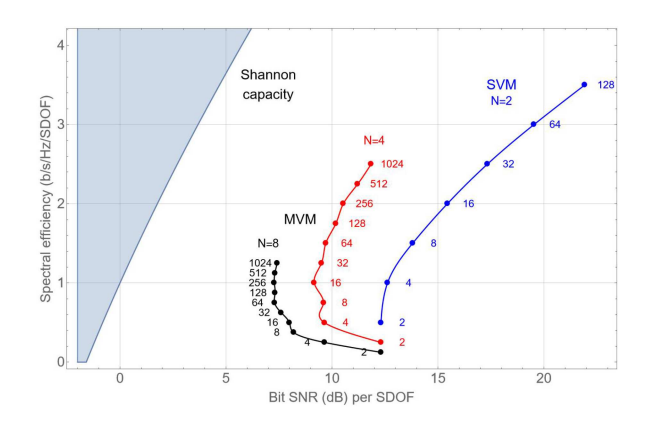


Fig. 18. MVM spectral efficiencies per SDOF vs the bit SNR per SDOF required to achieve a bit error probability of 10^{-4} for different degrees of freedom N and constellation cardinalities M. Blue, red, and black curves correspond to N=2,4,8, respectively. The number listed next to each point corresponds to the constellation cardinality.

G. MVM Performance for Various (N, M) Pairs

In this subsection, we examine the performance of geometrically-optimized signal sets that correspond to the densest sphere packing in the generalized Stokes space. We show that the best trade-off between spectral and energy efficiency occurs for simplex constellations.

Fig. 18 shows the MVM spectral efficiency per SDOF vs the bit SNR per SDOF required to achieve a bit error probability of 10^{-4} . Each curve corresponds to a different degree of freedom N, and each point marked on a curve corresponds to a different constellation cardinality M. It is worth mentioning that these graphs represent the performance of geometrically-shaped constellations with optimized bit-to-symbol mappings. Curves for non-optimized constellations lie on the right of these graphs. Furthermore, the apex (leftmost point) of each graph in Fig. 18 corresponds to a simplex constellation. Apparently, the best combination of spectral efficiency per SDOF and receiver sensitivity is achieved for SIC-POVMs. Higher spectral efficiencies can be obtained with a modest bit SNR penalty by switching to a constellation with more points, especially in higher-dimensional settings.

For the qualitative interpretation of results of Fig. 18, we need to take a closer look at the evaluation of error probability.

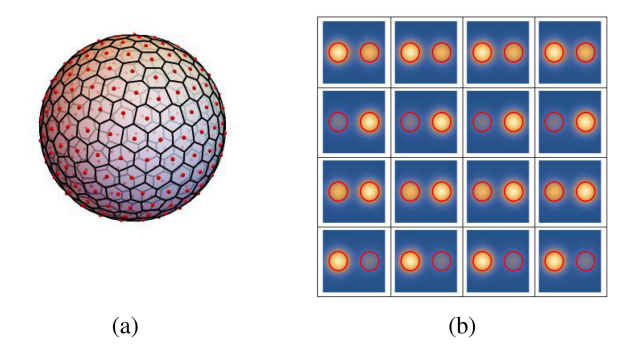


Fig. 19. (a) Optimized constellation and spherical Voronoi cells for N=2, M=256, obtained by solving the Thomson problem; (b) Intensity plots of the optimal MVM signal set for N=4, M=16, over a two-core multicore fiber with identical uncoupled single-mode cores.

The leading term of the asymptotic expression for the pairwise symbol error probability based on the union bound is given by (37).

For M>N, the Welch-Rankin bound on γ is written as [93] $\gamma \geq \sqrt{(M-N)/N(M-1)}$. This bound is not tight when the signal set cardinality tends to infinity. Below, we estimate γ from geometric arguments.

Fig. 19 shows the optimal Thomson constellation and the partitioning of the sphere into Dirichlet (Voronoi) cells for N=2, M=256. In general, for N=2 with large M, the Dirichlet cells for an optimal configuration are roughly hexagonal [90]. For simplicity, let us assume that the constellation points form an ideal hexagonal lattice. The Dirichlet cell for a two-dimensional hexagonal lattice is a regular hexagon of side $d/\sqrt{3}$, where d is the minimum Euclidean distance between pairs of points. The area of each cell is $\delta A = \sqrt{3}d^2/2$. We can estimate d if we divide the area of the unit sphere S^2 , equal to $A=4\pi$, by the total area of M cells. We obtain the estimate $d^2 \approx 8\pi/(\sqrt{3}M)$. We observe that, in the asymptotic limit of large M, the Euclidean distance is inversely proportional to the square root of the number of points M. By combining the formulas [75] $d^2 = \|\hat{s} - \hat{s}'\|^2 = 2(1 - \hat{s} \cdot \hat{s}'), \gamma^2 = |\langle s|s'\rangle|^2 =$ $(1 + \hat{s} \cdot \hat{s}')/2$, and using the first-order Taylor expansion of the square root of γ^2 , we obtain the average symbol error probability $\bar{P}_{e|s} \sim \exp[-\pi \gamma_s/(2\sqrt{3}M)].$

The average bit error probability for a Gray-like bit-to-symbol mapping is related to the average symbol error probability by $\bar{P}_{e|b}\simeq\bar{P}_{e|s}/k$, where $k:=\log_2\,M$. For quasi-orthogonal signal sets, it is related by $\bar{P}_{e|b}\simeq M\bar{P}_{e|s}/[2(M-1)]\simeq\bar{P}_{e|s}/2$. Gray-like bit-to-symbol mappings are expected at large constellation cardinalities M, while orthogonal signal sets exist for M< N and quasi-orthogonal signal sets occur for $N< M< N^2$. In general, the difference in SNR between the different bit-to-symbol mappings is asymptotically small. For the purposes of qualitatively understanding the results shown in Fig. 18, it is reasonable to assume that $\bar{P}_{e|b}\simeq\bar{P}_{e|s}$.

The spectral efficiency per SDOF for MVM is defined as $\eta := k/N$ and the symbol SNR per SDOF is related to the bit SNR per SDOF via $\gamma_s := k\gamma_b$. For a given average bit error

probability, we can write for N=2 (SVM case) that

$$\eta \sim \frac{\gamma_b(\mathrm{dB})}{20\log 2}.$$
(59)

Using a similar geometric argument for N>2 (MVM case), we find that $d^2 \sim M^{-\frac{1}{N-1}}$ and we can write

$$\eta \sim \frac{N-1}{N} \frac{\gamma_b(\mathrm{dB})}{10 \log 2}.$$
 (60)

Rephrasing the above expressions, we expect that the slope $\eta/\gamma_b(dB)\sim 0.16$ for N=2 at large constellation cardinalities M and that it will increase towards 0.33 as $N\to\infty$, which is approximately the slope of the Shannon capacity formula for AWGN.

At the opposite extreme, $\gamma=0$ for orthogonal signal sets with M< N and we expect that

$$\eta \sim 10^{-\gamma_b(\text{dB})/10}.$$
(61)

Using the preceding asymptotic analysis, we consider the results shown in Fig. 18. The MVM spectral efficiency η is generally expected to follow a C-shaped curve when plotted against the bit SNR per SDOF γ_b (dB). The upper part of the curve will increase linearly with the bit SNR per (59) and (60), while the lower part of the curve will decrease exponentially with the bit SNR per (61). Each curve's apex occurs for the simplex constellation with $M=N^2$, where $\gamma^2=(N+1)^{-1}$. We thus conclude that the simplex constellations offer the best balance between energy and spectral efficiency for N>2. An example of a simplex signal set for N=4 and M=16 is shown in Fig. 19(b).

From Fig. 17, we observe that (16,256)-MVM offers 7.2 dB better energy efficiency for an error probability of 10^{-9} compared to the binary SVM for the same spectral efficiency (0.5 b/s/Hz/SDOF). This is due to the fact that geometrically-shaped (16,256)-MVM has a configuration of constellation points in the 16D Jones space with a larger minimal distance. From Fig. 18, we also notice that, as the spectral efficiency per SDOF increases, increasing the dimensionality N of the MVM is increasingly beneficial from the energy efficiency point of view. Transmitting an SVM superchannel offers no such benefit.

H. Spectral Efficiency vs Energy Efficiency Trade-Offs

In Fig. 20, we plot the change in spectral efficiency per SDOF for SIC-POVM (simplex) MVM for different N as a function of the bit SNR per SDOF required to achieve a bit error probability of 10^{-4} (in blue). In the same figure, we graph Shannon's formula for the spectral efficiency of an AWGN channel (in red) [9]. The maximum spectral efficiency for the simplex MVM is equal to 1.06 b/s/Hz/SDOF and occurs for N=3. Similarly, the spectral efficiency for N=2 and N=4 is 1 b/s/Hz/SDOF. This means that, at best, the spectral efficiency of the simplex MVM is approximately equal to that of binary intensity modulation per SDOF for low N's and decreases thereafter with increasing N.

Notice that the simplex MVM DD over SDM fibers offers 6.6 dB sensitivity improvement compared to the conventional

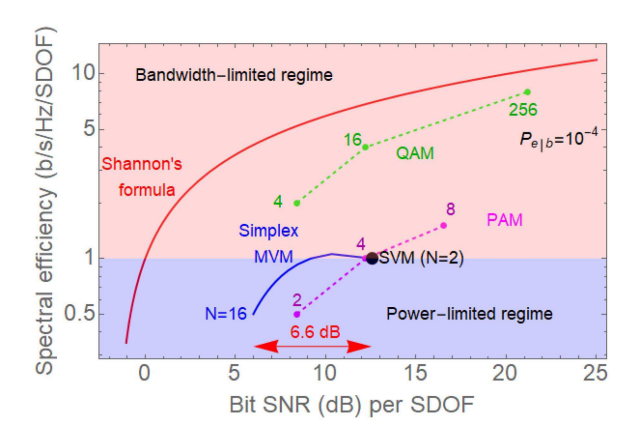


Fig. 20. SIC-POVM MVM spectral efficiencies per SDOF vs the bit SNR per SDOF required to achieve a bit error probability of 10^{-4} (in blue). Results for coherent PAM, QAM, and for SVM DD for various constellation cardinalities are also shown in magenta, green, and black, respectively.

TABLE I
COMPARISON OF DIFFERENT TRANSMISSION SCHEMES IN TERMS OF
IMPLEMENTATION AND COMPUTATIONAL COMPLEXITY

Transmission scheme	Single-channel MVM	Parallel SVM channels (SVM superchannel)
Cores per channel	K	1
SDOFs per channel	2N	2
Constellation cardinality per channel	M	$M^{1/K}$
Spectral efficiency per SDOF	$(\log_2 M)/N$	$(\log_2 M)/N$
Number of photodiodes	Conventional: $2N^2 - N$ Simplified-1: $5N - 4$ Simplified-2: $3N - 2$	3N
Number of ADC's	Conventional: N^2 Simplified-1: $3N - 2$ Simplified-2: $3N - 2$	$\frac{3N}{2}$
Computational complexity	LMS: $\mathcal{O}(N^4)$ ML: $\mathcal{O}(MN^2)$	$\frac{3N}{2}$

(Terminology: Simplified-1: MVM DD receiver architecture with linearized hardware complexity and balanced photodetectors after each 90-degree optical hybrid [69]; Simplified-2: Configuration composed exclusively of asymmetric 90-degree optical hybrids and single-ended photodetectors (unpublished)).

simplex SVM over SMFs (N=2), at the expense of spectral efficiency per SDOF.

Based on our analysis, we conclude that using MVM DD over SDM fibers could potentially be beneficial, since the spatial degrees of freedom in SDM fibers are utilized as one channel instead of as individual channels, as is standard engineering practice. In comparison to SVM DD over SMFs, MVM offers a greater degree of flexibility for balancing energy consumption and spectral efficiency.

VIII. COMMERCIAL VIABILITY OF MVM DD SYSTEMS

This section provides a point-by-point comparison of MVM in relation to other modulation formats considered for short-haul optical links. For the comparison, we use two performance metrics (spectral efficiency and bit SNR) and quantify the hardware complexity (in terms of component count, i.e., number of photodiodes/transimpedance amplifiers (TIAs) and ADCs) and the computational complexity (in terms of real multiplications per received symbol).

Table I compares the above metrics for a superchannel composed of SVM tributaries vs a single MVM channel using all available SDOFs. For an objective comparison, the aggregate data rate is the same in both cases.

For the comparison, without loss of generality, we consider a homogeneous multicore fiber with K single-mode cores. Thus, we have at our disposition $N=2\,K$ SDOFs.

For a given number of SDOFs N, MVM signals reside in a N-dimensional Jones space. In contrast, for a superchannel composed of K=N/2 SVM tributaries, the signals corresponding to each individual SVM tributary reside in a 2D Jones space. The composite constellation of the SVM superchannel is the Cartesian product of K SVM constellations. For a fair comparison, if M is the MVM constellation cardinality, we assume that the K=N/2 SVM tributaries have individual constellation cardinalities $M^{1/K}$. This gives the same spectral efficiency per SDOF equal to $(\log_2 M)/N$.

If we use the conventional Stokes vector DD receiver with three balanced photodiode pairs [27], we need 6 photodiodes per SDOF. Therefore, we need 6 K photodiodes to transmit Kindependent SVM channels in parallel over the K cores. Since N=2K, this transmission technique requires 3N photodiodes in total. We want to compare this number of photodiodes to the number of photodiodes we need to send a single MVM channel using N degrees of freedom. The simple naive generalization of the conventional Stokes vector DD receiver architecture from two to N dimensions uses $\mathcal{O}(N^2)$ photodiodes due to the fact that the dimension of the generalized Stokes space increases quadratically with the number of SDOFs, i.e., as $N^2 - 1$ [69]. The simplified MVM DD receiver architecture shown in Fig. 4(b), which was proposed by the authors in [69], takes into account the interdependence of the Stokes parameters to reduce the hardware complexity. The complexity increases linearly with the number of $\mathcal{O}(N)$ degrees of freedom [69]. This receiver uses N-1 optical hybrids with two balanced receivers each, i.e., 4 photodiodes per hybrid. In addition, it uses N single-ended photodiodes to measure the optical powers of the N SDOFs. Therefore, a total of 5N-4 photodiodes are required. However, we can employ a simplified version of the previous MVM DD receiver that uses 3N-2 single-ended photodiodes instead of the configuration using 5N-4 photodiodes. This is achieved by using exclusively asymmetric 90-degree optical hybrids and single-ended photodetectors at the four output ports of each hybrid. This receiver configuration eliminates the need for Nsingle-ended photodiodes to measure the optical powers of the NSDOFs. A different version of a reduced-hardware-complexity receiver for SVM can be found in [41], [45].

In both aforementioned MVM DD receiver configurations, 3N-2 ADCs are necessary. This number should be compared to the number of required ADCs in the SVM DD receiver case, i.e., 3K=3N/2. In other words, for large values of N, we need twice the number of ADCs when sending an MVM channel versus a superchannel composed of K SVM tributaries. This is the price we have to pay to gain in receiver sensitivity.

We assume that the LMS algorithm shown in Fig. 5 is used to derotate the transfer matrix of the fiber in the generalized Stokes space. There are two phases of operation, i.e., the training phase

Aggregate	Modulation	Spatial	Net symbol rate (GBd)	
bit rate	format	lanes	per lane	
400 Gbps	PAM 4	8 fibers	25	
	(2,4)-SVM	8 cores	25	
	(4,16)-MVM	4 core pairs	25	
	(8,256)-MVM	2 core tetrads	25	
800 Gbps	PAM 4	8 fibers	50	
	(2,4)-SVM	8 cores	50	
	(4,16)-MVM	4 core pairs	50	
	(8,256)-MVM	2 core tetrads	50	
	•			
1.6 Tbps Scenario 1	PAM 4	8 fibers	100	
	(2,4)-SVM	8 cores	100	
	(4,16)-MVM	4 core pairs	100	
	(8,256)-MVM	2 core tetrads	100	
	PAM 4	16 fibers	50	
1.6 Tbps	(2,4)-SVM	16 cores	50	
Scenario 2	(4,16)-MVM	8 core pairs	50	
	(8,256)-MVM	4 core tetrads	50	

TABLE II
CAPACITY UPGRADE SCENARIOS FOR FUTURE DATACENTER OPTICAL
INTERCONNECTS

and the decision-directed phase. During the training phase, the transfer matrix of the fiber is computed using training symbols. During the decision-directed phase, the LMS algorithm uses symbol decisions to track and counteract small fiber rotations that occurred since the training phase.

For the comparison of the computational complexity for a superchannel composed of SVM tributaries per lane vs a single MVM channel using all available SDOFs, we ignore the training phase and we take into account only the number of multiplications during the decision-directed phase.

The received generalized Stokes vector at the n-th instant is represented as a column vector $\vec{r}(n)$ with N^2-1 elements. The equalizer Müller matrix has dimensions $(N^2-1)\times (N^2-1)$. To generate each one of the components of the output generalized Stokes vector $\vec{z}(n)$, using a simple algorithm for matrix multiplication, requires $\mathcal{O}(N^2)$ real multiplications. Since $\vec{z}(n)$ has N^2-1 elements, we need $\mathcal{O}(N^4)$ real multiplications per received symbol.

Furthermore, for symbol decisions, we use the ML criterion, where $\vec{z}(n)$ is compared to all M nominal Stokes vectors representing the MVM alphabet symbols using the distance metric (24). We need $\mathcal{O}(N^2)$ real multiplications per dot product, i.e., $\mathcal{O}(MN^2)$ real multiplications per received symbol.

We note that the above simplified analysis does not take into account the non-linear interdependences of the components of the Stokes vectors and Müller matrices involved, which offer a path to complexity reduction (much like we did for the diode count at the receiver).

Various capacity upgrade scenarios for future datacenter optical interconnects are shown in Table II. Quad Small Form Factor Pluggable Double-Density (QSFP-DD) 400 GbE transceivers that use 8 fiber lanes with 50 Gb/s net bit rate per lane and PAM4 modulation are commercially available. It is expected that QSFP-DD 800 GbE and 1.6 TbE transceivers based on

8 and 16 fiber lanes, respectively, with 100 Gb/s net bit rate per lane and PAM4 modulation will be manufactured soon. In the more distant future, it is expected that 1.6TbE transceivers that use 8 fiber lanes, 200 Gb/s net bit rate per lane, and PAM4 modulation will be commercialized. Transceivers based on lite coherent detection technology that will support multi-TbE intra- and inter-data-center links are further down the road.

Table II also includes a few alternative SVM/MVM options for 400 GbE-1.6 TbE using 2/4/8 SDOFs. Can these solutions prevail over M-PAM? We can infer the performance advantages of these schemes by reviewing experimental results of recent SVM DD publications.

Feasibility experiments in the SVM literature that modulate all Stokes parameters simultaneously [33], [34] have achieved spectral efficiencies of 6 b/s/Hz and above 300 Gb/s per SVM channel. We conclude that, at least in principle, we can exceed the 200 Gb/s net bit rate per lane that seems to be the practical limit of the PAM4 technology.

It is worth emphasizing that the MVM concept can be equally well implemented using different sets of fully degenerate degrees of freedom other than SDOFs. In the ASE-noise-limited regime, in the absence of other transmission impairments, there is an equivalence in performance among systems using spatial and polarization modes and systems using other degrees of freedom, e.g., in the time domain (time slots), frequency domain (wavelength channels), or hybrid modes (combinations of the above). A hybrid space/time MVM implementation for N=4 was reported for the first time by Morsy-Osman et al. [32], where two SOPs and two time-slots were used jointly to achieve transmission of 320 Gb/s over 10 km of SMF using HD-FEC and 360 Gb/s over 20 km of SMF using SD-FEC.

Notice that the SVM constellations used in the above experiments [32], [33], [34] were not optimized. Optimized SVM constellations based on the face-centered cubic (FCC) lattice [40] with 16 and 64 points achieved 4 and 6 dB improved receiver sensitivity at SER of 10^{-5} compared to DP-PAM4 and DP-PAM8, respectively.

Can MVM-based optical interconnects compete with their coherent detection counterparts? It is clear that coherent detection is superior to any direct-detection scheme, both in sensitivity and DSP capabilities, for any modulation format. Therefore, SVM/DD and MVM/DD are proposed as intermediate solutions in terms of performance between *M*-PAM/DD and DP-16-QAM/coherent optical interconnects.

The closest SVM/MVM variant to coherent detection is to transmit an unmodulated carrier on one of the SDOFs and use this carrier to perform self-homodyning of the remaining SDOFs, like in [29], [30], [31], [53]. As mentioned above, this self-homodyne technique enables the use of more spectrally-efficient modulation formats, such as 16-QAM, and enables electronic chromatic dispersion compensation. This is not the case for *M*-PAM/DD, SVM/DD, and MVM/DD, where chromatic dispersion compensation should be achieved either optically, using a dispersion compensating fiber or working in the O-band, or using electronic pre-compensation.

IX. CONCLUSION

In this article, we investigated the merits of MVM with equipower signal sets, which is a direct extension of PolSK for the generalized Stokes space. In other words, we limited ourselves to a subset of the full spatial modulation/direct-detection family set. We derived an analytical upper limit for the back-to-back performance of M-ary MVM over N spatial degrees of freedom in the amplified spontaneous emission (ASE) noise-limited regime.

We also elaborated on the following topics: (i) The optimal MVM transceiver architecture; (ii) The use of simplex MVM constellations based on SIC-POVM vectors; (iii) The design of M-ary geometrically-shaped constellations obtained by numerical optimization of various objective functions using the method of gradient descent; and (iv) The optimal bit-to-symbol mapping using simulated annealing.

We showed that it is potentially beneficial to use MVM DD over SDM fibers, i.e., to use spatial degrees of freedom in SDM fibers together as a single channel instead of individually as separate channels, per standard engineering practice. Compared to SVM DD over SMFs, MVM DD over SDM fibers offers greater flexibility for better trade-offs between energy consumption and spectral efficiency.

The successful commercialization of MVM eventually depends on technoeconomics. MVM, like other advanced direct-detection techniques for spectrally-efficient transmission [12], [13], [14], [27], requires several parallel optical branches followed by ADCs and DSP, all of which increase cost and energy consumption in comparison to *M*-ary PAM and approach or even exceed the complexity of coherent receivers. Therefore, MVM's future commercial viability depends on the development of inexpensive silicon photonic (SiP) integrated circuits and application-specific integrated circuits (ASICs) for DSP.

APPENDIX A PAIRWISE SYMBOL ERROR PROBABILITY

The goal of this appendix is to compute the pairwise error probability $P_{\rm e,bin}^{m'|m}$ defined by (28) and prove (30).

The starting point for the analytical calculation of the pairwise symbol error probability is the maximum-likelihood decision criterion (24). This criterion, in turn, results in comparing the square magnitude of the projections of the received Jones vector $|r\rangle$ on a pair of nominal Jones vectors $|s\rangle$, $|s'\rangle$ representing transmitted MVM symbols and choosing the largest one. However, the vectors $|s\rangle$, $|s'\rangle$ are not orthogonal, in general. To facilitate the derivation of a closed formula for the pairwise symbol error probability, we use an orthogonal coordinate system described by the unit Jones vectors $|u_{\pm}\rangle$. These new vectors are the result of *symmetrically opening up* $|s'\rangle$ and $|s\rangle$ to be orthogonal.

We assume that the amplifier noise vector $|n\rangle$ that affects the received Jones vector $|r\rangle$ has spatial and polarization components that are independent and identically distributed Gaussian complex random variables. The magnitudes of the projections of the received Jones vector $|r\rangle$ on the unit Jones vectors $|u_\pm\rangle$ result in two independent random variables following Rice distributions. From that point, we can directly derive a closed form

expression for the pairwise symbol error probability. The final result is identical to the formula for the error probability of the envelope detection of correlated binary signals [9].

A. Geometric Setup

We fix $m \neq m'$ and, to simplify expressions, set $|s\rangle := |s_m\rangle$ and $|s'\rangle := |s_{m'}\rangle$. We assume that

$$\langle s|s\rangle = \langle s'|s'\rangle = 1,$$
 (62a)

$$\gamma := \langle s|s'\rangle > 0. \tag{62b}$$

In (62b), we dropped the absolute value on $\langle s|s'\rangle$ because, since we deal with two vectors in isolation and only the projection operators $\mathbf{S} = |s\rangle\langle s|$ and $\mathbf{S}' = |s'\rangle\langle s'|$ matter, we can adjust the phase of $|s'\rangle$ so that $\langle s|s'\rangle$ is a positive real. As the first step, we reduce the considerations to the two-dimensional complex subspace Σ spanned by $|s\rangle$ and $|s'\rangle$ and derive analytical expressions in a convenient orthonormal basis for Σ .

We express $P_{e,\text{bin}}^{m'|m}$ as

$$P_{\text{e,bin}}^{m'|m} = P\left(|\langle r|s'\rangle|^2 - |\langle r|s\rangle|^2 \ge 0\right)$$
$$= P\left(\langle r|\Delta|r\rangle \ge 0\right), \tag{63}$$

where we introduced the difference of dyads $\Delta := S' - S$ and the associated quadratic form⁴

$$|\langle r|s'\rangle|^2 - |\langle r|s\rangle|^2 = \operatorname{tr}(\mathbf{RS}') - \operatorname{tr}(\mathbf{RS}) = \operatorname{tr}(\mathbf{R\Delta})$$
$$= \langle r|\mathbf{\Delta}|r\rangle. \tag{64}$$

The following three real *length parameters* will play a key role:

$$\delta := \sqrt{1 - \gamma^2},\tag{65a}$$

$$\rho_{\pm} := \sqrt{\frac{1 \pm \delta}{2}}.\tag{65b}$$

For ease of reference we record that

$$\gamma = \sqrt{1 - \delta^2} = 2\rho_+ \rho_-,$$
 (66a)

$$\rho_{\pm} - \rho_{\mp} \gamma = (1 - 2\rho_{\mp}^2)\rho_{\pm} = \pm \delta \rho_{\pm}.$$
 (66b)

We also introduce two vectors in Σ , $|u_+\rangle$ and $|u_-\rangle$, defined

$$|u_{\pm}\rangle := \pm \frac{\rho_{\pm}|s'\rangle - \rho_{\mp}|s\rangle}{\delta}.$$
 (67)

Their scalar components along $|s'\rangle$ and $|s\rangle$ are found, via (66a) and (66b), to be

$$\langle s'|s'\rangle u_{\pm} = \pm \frac{\rho_{\pm} - \rho_{\mp}\gamma}{\delta} = \rho_{\pm},$$
 (68a)

$$\langle s|s\rangle u_{\pm} = \pm \frac{\rho_{\pm}\gamma - \rho_{\mp}}{\delta} = \rho_{\mp}.$$
 (68b)

Computing $\Delta |u_{\pm}\rangle$ as the difference of the projections onto $|s'\rangle$ and $|s\rangle$ (and then using (67)) gives

$$\Delta |u_{+}\rangle = \rho_{+}|s'\rangle - \rho_{\pm}|s\rangle = \pm \delta |u_{+}\rangle. \tag{69}$$

⁴Note that this formulation makes it clear that $\mathcal{D}^{m'|m}$ is bounded by 3D-cone in Σ treated as a 4D real space.

Thus, $|u_{\pm}\rangle$ are eigenvectors of Δ with eigenvalues $\pm\delta$, respectively. They are normalized since combining (67) and (68a), (68b) yields

$$\langle u_{\pm}|u_{\pm}\rangle = \pm \frac{1}{\delta} \langle (\rho_{\pm}|s'\rangle - \rho_{\mp}|s\rangle) |u_{\pm}\rangle$$
$$= \pm \frac{1}{\delta} (\rho_{\pm}^2 - \rho_{\mp}^2) = 1. \tag{70}$$

Because Δ is Hermitian of rank two, the eigenvectors $|u_\pm\rangle$ are orthogonal and the remaining eigenvalue of Δ , other than $\pm\delta$, is zero (with the orthogonal complement Σ^\perp as its eigenspace). The underlying geometry is simple: Examining (67), we see that $|u_\pm\rangle$ sit in the real sub-plane inside Σ spanned by $|s'\rangle$ and $|s\rangle$. The vectors $|s'\rangle$ and $|s\rangle$ form an acute angle (by virtue of our initial phase rotation). From (68a) and (68b), $\langle s'|u_+\rangle = \rho_+ = \langle s|u_-\rangle$, so this acute angle is positioned symmetrically within the right angle formed by $|u_\pm\rangle$. One could say that $|u_\pm\rangle$ are the result of symmetrically opening up $|s'\rangle$ and $|s\rangle$ to be orthogonal.

B. Signal Decomposition

With our orthonormal basis $|u_{\pm}\rangle$ of Σ in hand, we orthogonally decompose the noise

$$|n\rangle = |n_{+}\rangle + |n_{-}\rangle + |\tilde{n}\rangle,\tag{71}$$

where the components along $|u_{\pm}\rangle$ are

$$|n_{+}\rangle := \langle n|u_{+}\rangle|u_{+}\rangle \tag{72a}$$

and

$$|n_{-}\rangle := \langle n|u_{-}\rangle|u_{-}\rangle,\tag{72b}$$

and $|\tilde{n}\rangle$ is the component orthogonal to Σ . (Going forward, tilde indicates components orthogonal to Σ .) Inverting (67), we get the analogous decomposition of the symbols

$$|s\rangle = \rho_-|u_+\rangle + \rho_+|u_-\rangle,\tag{73a}$$

$$|s'\rangle = \rho_+|u_+\rangle + \rho_-|u_-\rangle. \tag{73b}$$

Because the Gaussian noise $|n\rangle$ is symmetric with respect to phase rotations, we can disregard the random phase in (10) and express the Jones vector representing the incoherently-received signal as $|r\rangle = |s\rangle + |n\rangle$. Putting together (71) and (73a), (73b), reveals its components along $|u_+\rangle$ as equal to

$$|r_{+}\rangle = \rho_{-}|u_{+}\rangle + |n_{+}\rangle,\tag{74a}$$

$$|r_{-}\rangle = \rho_{+}|u_{-}\rangle + |n_{-}\rangle,\tag{74b}$$

with the squared magnitudes consequently given by

$$\langle r_{\pm}|r_{\pm}\rangle = \rho_{\pm}^2 + 2\rho_{\mp}\Re\langle n_{\pm}|u_{\pm}\rangle + \langle n_{\pm}|n_{\pm}\rangle. \tag{75}$$

The full $|r\rangle$ decomposes into orthogonal components,

$$|r\rangle = |s\rangle + |n\rangle = |r_{+}\rangle + |r_{-}\rangle + |\tilde{r}\rangle,$$
 (76)

along the eigenspaces of Δ for eigenvalues δ , $-\delta$, and 0, respectively.

Using $\Delta |\tilde{r}\rangle = 0$ as well as $\Delta |r_{\pm}\rangle = \pm \delta |r_{\pm}\rangle$ and $\langle r_{-}|r_{+}\rangle = 0$, the quadratic form simplifies to

$$\langle r|\mathbf{\Delta}|r\rangle = \langle |r_{+}\rangle + |r_{-}\rangle + |\tilde{r}\rangle |\mathbf{\Delta}| |r_{+}\rangle + |r_{-}\rangle + |\tilde{r}\rangle \rangle$$

$$= \langle r_{+}|\mathbf{\Delta}|r_{+}\rangle + \langle r_{-}|\mathbf{\Delta}|\mathbf{r}_{-}\rangle$$

$$= \delta \langle r_{+}|r_{+}\rangle - \delta \langle r_{-}|r_{-}\rangle. \tag{77}$$

Finally, substituting (75), yields

$$\langle r|\mathbf{\Delta}|r\rangle = t\delta \left[\rho_{-}^{2} - \rho_{+}^{2} + 2\Re\left\{\rho_{-}\langle u_{+}|n_{+}\rangle\right.\right.$$
$$\left. - \rho_{+}\langle u_{-}|n_{-}\rangle\right\}$$
$$\left. + \langle n_{+}|n_{+}\rangle - \langle n_{-}|n_{-}\rangle\right]. \tag{78}$$

Apart form the signal terms ρ_{\mp} , the last expression includes fluctuations resulting from signal-ASE noise and ASE noise-ASE noise beatings.

C. Pairwise Symbol Error Probability Calculation

We are ready to derive the closed form (30) for $P_{\rm e,bin}^{m'|m}$ by identifying the relevant probability distributions associated to the quadratic form. We can describe the points of Σ by their components $x_- + \iota y_-$ and $x_+ + \iota y_+$ with respect to the orthonormal basis $|u_{\mp}\rangle$. Accordingly, we have four independent real Gaussian random variables with variance σ^2 :

$$x_{\mp} := \Re \langle n | u_{\mp} \rangle \tag{79a}$$

and

$$y_{\pm} := \Im \langle n | u_{\pm} \rangle. \tag{79b}$$

The last equation of the previous section, (78), reads

$$\frac{1}{\delta} \langle r | \mathbf{\Delta} | r \rangle = \rho_{-}^{2} - \rho_{+}^{2} + 2\rho_{-} x_{+} - 2\rho_{+} x_{-} + x_{\perp}^{2} + y_{\perp}^{2} - x_{-}^{2} - y_{\perp}^{2}.$$
(80)

So, upon completing the squares, the sought pairwise error probability in (63) is

$$P_{\text{e,bin}}^{m'|m} = P\left(\langle r|\mathbf{\Delta}|r\rangle \ge 0\right)$$

$$= P\left[(\rho_{-} + x_{+})^{2} + y_{+}^{2} \ge (\rho_{+} + x_{-})^{2} + y_{-}^{2}\right]. \quad (81)$$

This is to say that

$$P_{\text{e,bin}}^{m'|m} = P(\psi_{-} \ge \psi_{+}),$$
 (82)

where we introduced two independent Rice-distributed random variables

$$\psi_{-} := \sqrt{(x_{+} + \rho_{-})^{2} + y_{+}^{2}}, \tag{83a}$$

$$\psi_{+} := \sqrt{(x_{-} + \rho_{+})^{2} + y_{-}^{2}},$$
 (83b)

with reference distances ρ_- and ρ_+ , respectively, and a common scale parameter σ . The PDFs of ψ_\pm are

$$f_{\pm}(x) = \frac{x}{\sigma^2} \exp\left(-\frac{x^2 + \rho_{\pm}^2}{2\sigma^2}\right) I_0\left(\frac{x\rho_{\pm}}{\sigma^2}\right),$$
 (84)

with the corresponding tail (complementary) distribution functions [9]

$$P(\psi_{\pm} \ge x) = Q_1\left(\frac{\rho_{\pm}}{\sqrt{\sigma^2}}, \frac{x}{\sqrt{\sigma^2}}\right). \tag{85}$$

Recall that Q_1 stands for the *Marcum function* defined by (32). Thus, formula (82) can be represented by a single integral:

$$P_{e,\text{bin}}^{m'|m} = \int_0^\infty P(\psi_- \ge x) f_+(x) dx$$

$$= \int_0^\infty Q_1 \left(\frac{\rho_-}{\sqrt{\sigma^2}}, \frac{x}{\sqrt{\sigma^2}}\right) \frac{x}{\sigma^2}$$

$$\exp\left(-\frac{x^2 + \rho_+^2}{2\sigma^2}\right) I_0 \left(\frac{x\rho_+}{\sigma^2}\right) dx. \tag{86}$$

The last integral can be computed in closed form [101]

$$\begin{split} P_{\rm e,bin}^{m'|m} &= P(\psi_- \ge \psi_+) \\ &= Q_1(\mathtt{a},\mathtt{b}) - \frac{1}{2} \exp\left(-\frac{\mathtt{a}^2 + \mathtt{b}^2}{2}\right) I_0(\mathtt{a}\mathtt{b}), \quad \ \ (87) \end{split}$$

where, recalling that $\gamma_s = \frac{1}{2\sigma^2}$ per (14), we set

$$\mathbf{a} := \frac{\rho_{-}}{\sqrt{2\sigma^2}} = \rho_{-}\sqrt{\gamma_s},\tag{88a}$$

$$b := \frac{\rho_+}{\sqrt{2\sigma^2}} = \rho_+ \sqrt{\gamma_s}. \tag{88b}$$

Using $\rho_-^2+\rho_+^2=1$ and $\rho_-^2\rho_+^2=\frac{1-\delta^2}{4}=\frac{\gamma^2}{4}$ from (65a) through (66b) gives

$$a^2 + b^2 = (\rho^2 + \rho_{\perp}^2)\gamma_s = \gamma_s,$$
 (89a)

$$2ab = 2\rho_-\rho_+\gamma_s = \gamma\gamma_s. \tag{89b}$$

Thus (87) coincides with the promised formula (30). \Box

APPENDIX B ASYMPTOTICS FOR LARGE SNRS

We derive the approximate formulas for the error probability stated in Corollary 2 and valid for large SNR parameters γ_s , as well as the simplified approximation (36).

The exact formula (30) reads

$$P_{\text{e,bin}}^{m'|m} = Q_1 \left(\rho_- \sqrt{\gamma_s}, \rho_+ \sqrt{\gamma_s} \right) - \frac{1}{2} \exp\left(-\frac{\gamma_s}{2} \right) I_0 \left(\frac{\gamma \gamma_s}{2} \right). \tag{90}$$

For large $x:=\frac{\gamma\gamma_s}{2}$, taking the first n+1 terms of the Hankel asymptotics given by [101]

$$I_0(x) = \frac{e^x}{\sqrt{2\pi x}} \left(1 + \frac{1}{8x} + \frac{1 \cdot 9}{2!(8x)^2} + \frac{1 \cdot 9 \cdot 25}{3!(8x)^3} + \dots \right),$$

yields an approximation to the Bessel term in (90):

$$\exp\left(-\frac{\gamma_s}{2}\right)I_0\left(\frac{\gamma\gamma_s}{2}\right) \sim g_n \exp\left[-\frac{\gamma_s(1-\gamma)}{2}\right],$$
 (91)

with

$$g_n := \frac{1}{\sqrt{\pi}} \left(\frac{1}{(\gamma \gamma_s)^{\frac{1}{2}}} + \frac{\frac{1}{4}}{(\gamma \gamma_s)^{\frac{3}{2}}} + \frac{\frac{9}{32}}{(\gamma \gamma_s)^{\frac{5}{2}}} + \dots \right), \quad (92)$$

where the sum is terminated on $\frac{(2n-1)!!^2}{4^n n!} \left(\gamma \gamma_s\right)^{-n-1/2}$ for $n \geq 1$. A similar asymptotic expansion for the Marcum function term $Q_1\left(\rho_-\sqrt{\gamma_s},\rho_+\sqrt{\gamma_s}\right)$ in (90) is more subtle and can be extracted from [82] in the form of a linear combination of the exponential $\exp[-\frac{\gamma_s(1-\gamma)}{2}]$ and the error function $\operatorname{erfc}\left(\frac{\sqrt{\gamma_s}\sqrt{1-\gamma}}{\sqrt{2}}\right)$ with the coefficients described below. (Here $\operatorname{erfc}(x):=\frac{2}{\sqrt{\pi}}\int_x^\infty e^{-t^2}\,dt.$) To start, define \mathbf{e}_n and \mathbf{f}_n recursively: Let $\mathbf{e}_0:=0$ and follow with

$$\mathbf{e}_n := \frac{1}{\frac{1}{2} - n} \left[\frac{1 - \gamma}{\gamma} \mathbf{e}_{n-1} - \left(\frac{\gamma \gamma_s}{2} \right)^{\frac{1}{2} - n} \right] \quad (n \ge 1). \quad (93)$$

Let $f_0 := \sqrt{\pi} \sqrt{\frac{\gamma}{1-\gamma}}$ and follow with

$$f_n := \frac{1}{\frac{1}{2} - n} \frac{1 - \gamma}{\gamma} f_{n-1} \quad (n \ge 1).$$
 (94)

Then, using constants

$$A_{n,m} := \frac{1}{n!2^n} \frac{\Gamma(\frac{1}{2} + m + n)}{\Gamma(\frac{1}{2} + m - n)} = \frac{1}{n!2^n} \prod_{i=-n}^{n-1} \left(m + i + \frac{1}{2} \right),$$
(95)

define a multiplier

$$\lambda_n := \frac{(-1)^n}{2\sqrt{2\pi}} \left(\frac{\rho_+}{\rho_-} A_{n,0} - A_{n,1} \right), \tag{96}$$

and set

$$\mathsf{e}'_n := \lambda_n \mathsf{e}_n, \tag{97a}$$

$$\mathbf{f}_n' := \lambda_n \mathbf{f}_n, \tag{97b}$$

$$\mathbf{e}_n'' := \sum_{i=0}^n \mathbf{e}_i',\tag{97c}$$

$$\mathbf{f}_n'' := \sum_{i=0}^n \mathbf{f}_i'. \tag{97d}$$

We note that \mathbf{f}''_n only depends on γ while \mathbf{e}''_n is a linear combination of the powers $(\gamma\gamma_s)^{-\frac{1}{2}}$, $(\gamma\gamma_s)^{-\frac{3}{2}}$, ..., $(\gamma\gamma_s)^{-\frac{2n-1}{2}}$ with γ -dependent coefficients (for $n \geq 1$).

The approximation given by formula (37) in [82] reads then

$$Q_1\left(\rho_-\sqrt{\gamma_s},\rho_+\sqrt{\gamma_s}\right)$$

$$\sim \mathbf{e}_n'' \exp \left[-\frac{\gamma_s(1-\gamma)}{2} \right] + \mathbf{f}_n'' \operatorname{erfc} \left(\frac{\sqrt{\gamma_s}\sqrt{1-\gamma}}{\sqrt{2}} \right).$$
 (98)

An important feature of (98) is that it is valid uniformly across $\gamma \in (0, 1)$ (as long as $\gamma \gamma_s$ is sufficiently large). In [84] explicit

error bounds are discussed together with suitable expansion termination criteria. For our purposes, using n=1 gives excellent results.

To approximate the error probability $P_{\rm e,bin}^{m'|m}$, as given by (90), we combine the Marcum and Bessel approximations, (98) and (91), and obtain:

$$P_{\rm e,bin}^{m'|m} \sim f_n'' \operatorname{erfc}\left(\frac{\sqrt{\gamma_s}\sqrt{1-\gamma}}{\sqrt{2}}\right) + \left(e_n'' - \frac{1}{2}g_n\right) \exp\left[-\frac{\gamma_s(1-\gamma)}{2}\right]. \tag{99}$$

Corollary 2 will follow now by using n = 0, 1 in (99).

To streamline formulas we reach back to (65a), (65b), and note

$$\frac{\rho_+}{\rho_-} = \frac{\sqrt{1+\delta}}{\sqrt{1-\delta}} = \frac{1+\delta}{\sqrt{1-\delta^2}} = \frac{1+\delta}{\gamma}.$$
 (100)

Also, squaring as follows

$$(\rho_{+} \pm \rho_{-})^{2} = \left(\sqrt{\frac{1+\delta}{2}} \pm \sqrt{\frac{1-\delta}{2}}\right)^{2} = 1 \pm \sqrt{1-\delta^{2}},$$
(101)

gives

$$\rho_{+} \pm \rho_{-} = \sqrt{1 \pm \gamma}.\tag{102}$$

In particular,

$$\frac{\rho_{+}}{\rho_{-}} - 1 = \frac{\rho_{+} - \rho_{-}}{\rho_{-}} = \sqrt{2}\sqrt{\frac{1 - \gamma}{1 - \delta}}.$$
 (103)

Taking n = 0, we find $A_{0,0} = 1$ and $A_{0,1} = 1$, so

$$\mathbf{f}_0'' = \mathbf{f}_0' = \lambda_0 \mathbf{f}_0 = \frac{1}{2\sqrt{2\pi}} \left(\frac{\rho_+}{\rho_-} - 1 \right) \sqrt{\pi} \sqrt{\frac{\gamma}{1 - \gamma}}$$
$$= \frac{1}{2} \sqrt{\frac{\gamma}{1 - \delta}}, \tag{104}$$

where we used (103). Plugging (104) and $e_0''=0$ and $g_0=(\gamma\gamma_s)^{-1/2}/\sqrt{\pi}$ (from (92)) into (99) reproduces (34), the first formula in Corollary 2:

$$P_{\text{e,bin}}^{m'|m} \sim \frac{1}{2} \sqrt{\frac{\gamma}{1-\delta}} \operatorname{erfc}\left(\frac{\sqrt{\gamma_s}\sqrt{1-\gamma}}{\sqrt{2}}\right) - \frac{1}{2\sqrt{\pi\gamma\gamma_s}} \exp\left[-\frac{\gamma_s(1-\gamma)}{2}\right]. \tag{105}$$

Taking n = 1, we find $A_{1,0} = -\frac{1}{8}$ and $A_{1,1} = \frac{3}{8}$, so

$$\mathbf{f}_{1}' = \mathbf{f}_{1}\lambda_{1} = \frac{1}{\frac{1}{2} - 1} \frac{1 - \gamma}{\gamma} \sqrt{\pi} \sqrt{\frac{\gamma}{1 - \gamma}} \frac{(-1)^{1}}{2\sqrt{2\pi}} \left(-\frac{\rho_{+}}{\rho_{-}} \frac{1}{8} - \frac{3}{8} \right)$$

$$= -\sqrt{\frac{1 - \gamma}{\gamma}} \frac{1}{8\sqrt{2}} \left(\frac{\rho_{+}}{\rho_{-}} + 3 \right)$$

$$= -\sqrt{\frac{1 - \gamma}{\gamma}} \frac{1}{8\sqrt{2}} \left(\frac{1 + \delta}{\gamma} + 3 \right), \tag{106}$$

where we used (100). Thus, using (104), we arrive with

$$\mathbf{f}_{1}'' = \mathbf{f}_{0}' + \mathbf{f}_{1}'$$

$$= \frac{1}{2} \sqrt{\frac{\gamma}{1 - \delta}} - \sqrt{\frac{1 - \gamma}{\gamma}} \frac{1}{8\sqrt{2}} \left(\frac{1 + \delta}{\gamma} + 3 \right). \tag{107}$$

Turning attention to $e_1'' = e_1' = e_1 \lambda_1$, we have

$$\mathbf{e}_{1}'' = \frac{1}{\frac{1}{2} - 1} \left(-\left(\frac{\gamma \gamma_{s}}{2}\right)^{\frac{1}{2} - 1} \right) \frac{(-1)^{1}}{2\sqrt{2\pi}} \left(-\frac{\rho_{+}}{\rho_{-}} \frac{1}{8} - \frac{3}{8} \right)$$

$$= \frac{1}{8\sqrt{\pi}} \left(\frac{\rho_{+}}{\rho_{-}} + 3\right) (\gamma \gamma_{s})^{-\frac{1}{2}}.$$
(108)

Fetching g_0 from (92) and then using (103) gives

$$e_{1}'' - \frac{1}{2}g_{0} = \frac{1}{8\sqrt{\pi}} \left(\frac{\rho_{+}}{\rho_{-}} + 3\right) (\gamma\gamma_{s})^{-\frac{1}{2}} - \frac{1}{2} \frac{1}{\sqrt{\pi}} (\gamma\gamma_{s})^{-\frac{1}{2}}$$

$$= \frac{1}{8\sqrt{\pi}} \left(\frac{\rho_{+}}{\rho_{-}} - 1\right) (\gamma\gamma_{s})^{-\frac{1}{2}}$$

$$= \frac{\sqrt{2}}{8\sqrt{\pi}} \sqrt{\frac{1-\gamma}{1-\delta}} (\gamma\gamma_{s})^{-\frac{1}{2}}.$$
(109)

Subtracting one more term of the Bessel expansion (92) yields

$$\mathbf{e}_{1}'' - \frac{1}{2}\mathbf{g}_{1} = \frac{\sqrt{2}}{8\sqrt{\pi}}\sqrt{\frac{1-\gamma}{1-\delta}} (\gamma\gamma_{s})^{-\frac{1}{2}} - \frac{1}{8\sqrt{\pi}} (\gamma\gamma_{s})^{-\frac{3}{2}}.$$
(110)

One can check now that plugging (110) and (107) into (99) reproduces (35), the second formula in Corollary 2.

Remark 1: Dropping the $(\gamma \gamma_s)^{-\frac{3}{2}}$ term in the second formula in Corollary 2 yields

$$P_{e,\text{bin}}^{m'|m} \sim \left[\frac{1}{2} \sqrt{\frac{\gamma}{1-\delta}} - \sqrt{\frac{1-\gamma}{\gamma}} \frac{1}{8\sqrt{2}} \left(\frac{1+\delta}{\gamma} + 3 \right) \right]$$

$$\cdot \operatorname{erfc} \left(\frac{\sqrt{\gamma_s} \sqrt{1-\gamma}}{\sqrt{2}} \right)$$

$$+ \frac{\sqrt{2}}{8\sqrt{\pi}} \sqrt{\frac{1-\gamma}{1-\delta}} \left(\gamma \gamma_s \right)^{-\frac{1}{2}} \exp \left[-\frac{\gamma_s (1-\gamma)}{2} \right]. \tag{111}$$

This is a somewhat looser approximation for very large γ_s but works well for moderate values of γ_s of interest in our applications.

It remains to derive the crude approximation (36). When $\sqrt{x} = \frac{\sqrt{\gamma_s}\sqrt{1-\gamma}}{\sqrt{2}}$ is large, which happens for large γ_s when γ is not too close to 1, the simple standard asymptotic form $\operatorname{erfc}(\sqrt{x}) \sim \frac{1}{\sqrt{\pi x}} e^{-x}$ is appropriate and, when substituted into (105), yields (36):

$$\begin{split} & P_{\mathrm{e,bin}}^{m'|m} \\ & \sim \frac{1}{2} \left[\sqrt{\frac{\gamma}{1-\delta}} \frac{\sqrt{2}}{\sqrt{\pi}\sqrt{\gamma_s}\sqrt{1-\gamma}} - \frac{1}{\sqrt{\pi\gamma\gamma_s}} \right] \exp\left[-\frac{\gamma_s(1-\gamma)}{2} \right] \\ & = \frac{1}{2} \left[\frac{\sqrt{2}\gamma}{\sqrt{1-\delta}\sqrt{1-\gamma}} - 1 \right] \frac{1}{\sqrt{\pi\gamma\gamma_s}} \exp\left[-\frac{\gamma_s(1-\gamma)}{2} \right] \end{split}$$

$$=\frac{1}{2}\frac{\sqrt{1+\gamma}}{\sqrt{1-\gamma}}\frac{1}{\sqrt{\pi\gamma\gamma_s}}\exp\left[-\frac{\gamma_s(1-\gamma)}{2}\right],\tag{112}$$

where the last equality can be obtained by using

$$\sqrt{1+\gamma} + \sqrt{1-\gamma} = \sqrt{2}\sqrt{1+\delta},\tag{113}$$

which itself is evident from $\delta=\sqrt{1-\gamma^2}$ after squaring. It is worth recording that (112) can be also rewritten as

$$P_{\rm e,bin}^{m'|m} \sim \frac{1}{\sqrt{2\pi}} \frac{\sqrt{1 + \frac{1}{1 - {\rm d_{ic}^2}/2}}}{{\rm d_{ic}}} \frac{1}{\sqrt{\gamma_s}} \exp\left(-\frac{1}{2}\gamma_s \frac{{\rm d_{ic}^2}}{2}\right),$$
(114)

where d_{ic} stands for $d_{ic}(s_m, s_{m'}) = \sqrt{2}\sqrt{1-\gamma}$, the incoherent distance between the two symbols s_m and $s_{m'}$ (as given by (41)). This explains the leading asymptotic behavior given in expression (37).

ACKNOWLEDGMENT

The authors would like to thank Prof. M. Karlsson of Chalmers University for bringing to their attention the decision criterion proposed by [25], [55].

REFERENCES

- D. V. Plant, M. H. Morsy-Osman, M. Chagnon, and S. Lessard, "Trends in high-speed interconnects for datacenter networking: Multidimensional formats and their enabling DSP," in *Optical Switching in Next Generation Data Centers*. Berlin, Germany: Springer, 2018, pp. 261–277.
- [2] X. Chen, C. Antonelli, A. Mecozzi, D. Che, and W. Shieh, "High-capacity direct-detection systems," in *Optical Fiber Telecommunications VII*. Amsterdam, The Netherlands: Elsevier, 2020, pp. 419–441.
- [3] M. H. Eiselt, A. Dochhan, and J.-P. Elbers, "Data center interconnects at 400G and beyond," in *Proc. 23rd Opto- Electron. Commun. Conf.*, 2018, pp. 1–2.
- [4] X. Pang et al., "200 Gbps/lane IM/DD technologies for short reach optical interconnects," J. Lightw. Technol., vol. 38, no. 2, pp. 492–503, Jan. 2020.
- [5] S. T. Le, K. Schuh, R. Dischler, F. Buchali, L. Schmalen, and H. Buelow, "Beyond 400 Gb/s direct detection over 80 km for data center interconnect applications," *J. Lightw. Technol.*, vol. 38, no. 2, pp. 538–545, Jan. 2020.
- [6] T. Wettlin, S. Calabro, T. Rahman, J. Wei, N. Stojanovic, and S. Pachnicke, "DSP for high-speed short-reach IM/DD systems using PAM," *J. Lightw. Technol.*, vol. 38, no. 24, pp. 6771–6778, Dec. 2020.
- [7] O. Ozolins et al., "100 Gbaud on-off keying/pulse amplitude modulation links in C-band for short-reach optical interconnects," *Appl. Sci.*, vol. 11, May 2021, Art. no. 4284.
- [8] Cisco, "Cisco Annual Internet report (2018–2023)," San Jose, CA, USA: Cisco Systems Inc., White Paper, Mar. 2020.
- [9] J. G. Proakis, *Digital Communications*, 5th ed. New York, NY, USA: McGraw Hill, 2007.
- [10] K.-P. Ho, Phase-Modulated Optical Communication Systems. Berlin, Germany: Springer, 2005.
- [11] S. Huard, *Polarization of Light*. Hoboken, NJ, USA: Wiley, 1997.
- [12] A. Mecozzi, C. Antonelli, and M. Shtaif, "Kramers-Kronig coherent receiver," Optica, vol. 3, no. 11, 2016, Art. no. 12201227.
- [13] Y. Yoshida, T. Umezawa, A. Kanno, and N. Yamamoto, "A phase-retrieving coherent receiver based on two-dimensional photodetector array," *J. Lightw. Technol.*, vol. 38, no. 1, pp. 90–100, Jan. 2019.
- [14] H. Chen, N. K. Fontaine, J. M. Gene, R. Ryf, D. T. Neilson, and G. Raybon, "Dual polarization full-field signal waveform reconstruction using intensity only measurements for coherent communications," *J. Lightw. Technol.*, vol. 38, no. 9, pp. 2587–2597, May 2020.

- [15] T. Ji, C. Sun, H. Ji, Z. Xu, Y. Peng, and W. Shieh, "Theoretical and experimental investigations of interleaved carrier-assisted differential detection," *J. Lightw. Technol.*, vol. 39, no. 1, pp. 122–128, Jan. 2021.
- [16] J. K. Perin, A. Shastri, and J. M. Kahn, "Data center links beyond 100 Gbit/s per wavelength," Opt. Fiber Technol., vol. 44, pp. 69–85, Aug. 2018.
- [17] J. K. Perin, A. Shastri, and J. M. Kahn, "Coherent data center links," J. Lightw. Technol., vol. 39, no. 3, pp. 730–741, Feb. 2021.
- [18] X. Zhou, R. Urata, and H. Liu, "Beyond 1 Tb/s intra-data center interconnect technology: IM-DD or coherent?," J. Lightw. Technol., vol. 38, no. 2, pp. 475–484, Jan. 2020.
- [19] M. Morsy-Osman et al., "DSP-free 'coherent-lite' transceiver for next generation single wavelength optical intra-datacenter interconnects," Opt. Exp., vol. 26, Apr. 2018, Art. no. 8890.
- [20] Z. Jia and L. A. Campos, "Coherent optics ready for prime time in short-haul networks," *IEEE Netw.*, vol. 35, no. 2, pp. 8–14, Mar./Apr. 2021.
- [21] G. R. Martella, A. Nespola, S. Straullu, F. Forghieri, and R. Gaudino, "Scaling laws for unamplified coherent transmission in next-generation short-reach and access networks," *J. Lightw. Technol.*, vol. 39, no. 18, pp. 5805–5814, Sep. 2021.
- [22] S. Betti, F. Curti, G. De Marchis, and E. Iannone, "Multilevel coherent optical system based on Stokes parameters modulation," *J. Lightw. Technol.*, vol. 8, no. 7, pp. 1127–1136, Jul. 1990.
- [23] S. Betti, G. De Marchis, and E. Iannone, "Polarization modulated direct detection optical transmission systems," *J. Lightw. Technol.*, vol. 10, no. 12, pp. 1985–1997, Dec. 1992.
- [24] S. Benedetto and P. Poggiolini, "Theory of polarization shift keying modulation," *IEEE Trans. Commun.*, vol. 40, no. 4, pp. 708–721, Apr. 1992.
- [25] S. Benedetto and P. Poggiolini, "Multilevel polarization shift keying: Optimum receiver structure and performance evaluation," *IEEE Trans. Commun.*, vol. 42, no. 234, pp. 1174–1186, Feb.–Apr. 1994.
- [26] S. Benedetto, R. Gaudino, and P. Poggiolini, "Direct detection of optical digital transmission based on polarization shift keying modulation," *IEEE J. Sel. Areas Commun.*, vol. 13, no. 3, pp. 531–542, Apr. 1995.
- [27] K. Kikuchi and S. Kawakami, "Multi-level signaling in the Stokes space and its application to large-capacity optical communications," *Opt. Exp.*, vol. 22, Mar. 2014, Art. no. 7374.
- [28] S. S. Cercós et al., "100 Gbps IM/DD links using quad-polarization: Performance, complexity, and power dissipation," *Opt. Exp.*, vol. 23, Jul. 2015, Art. no. 19954.
- [29] D. Che, A. Li, X. Chen, Q. Hu, Y. Wang, and W. Shieh, "Stokes vector direct detection for linear complex optical channels," *J. Lightw. Technol.*, vol. 33, no. 3, pp. 678–684, Feb. 2015.
- [30] D. Che and W. Shieh, "Polarization demultiplexing for Stokes vector direct detection," *J. Lightw. Technol.*, vol. 34, no. 2, pp. 754–760, Jan. 2016.
- [31] P. Dong, X. Chen, K. Kim, S. Chandrasekhar, Y.-K. Chen, and J. H. Sinsky, "128-Gb/s 100-km transmission with direct detection using silicon photonic Stokes vector receiver and I/Q modulator," *Opt. Exp.*, vol. 24, Jun. 2016, Art. no. 14208.
- [32] M. Morsy-Osman, M. Chagnon, and D. V. Plant, "Four-dimensional modulation and Stokes direct detection of polarization division multiplexed intensities, inter polarization phase and inter polarization differential phase," *J. Lightw. Technol.*, vol. 34, no. 7, pp. 1585–1592, Apr. 2016.
- [33] M. Chagnon, M. Morsy-Osman, D. Patel, V. Veerasubramanian, A. Samani, and D. Plant, "Digital signal processing for dualpolarization intensity and interpolarization phase modulation formats using Stokes detection," *J. Lightw. Technol.*, vol. 34, no. 1, pp. 188–195, Jan. 2016.
- [34] M. Chagnon, M. Morsy-Osman, and D. V. Plant, "Multi-dimensional formats and transceiver architectures for direct detection with analysis on inter-polarization phase modulation," *J. Lightw. Technol.*, vol. 35, no. 4, pp. 885–892, Feb. 2017.
- [35] M. Y. S. Sowailem et al., "Impact of chromatic dispersion compensation in single carrier two-dimensional Stokes vector direct detection system," *IEEE Photon. J.*, vol. 9, no. 4, pp. 1–10, Aug. 2017.
- [36] S. Ishimura and K. Nishimura, "DSP technologies in the Stokes vector receivers for short-reach optical transmission systems," *Proc. SPIE*, vol. 10560, pp. 26–31, 2018.
- [37] S. Ghosh, T. Tanemura, Y. Kawabata, K. Katoh, K. Kikuchi, and Y. Nakano, "Decoding of multilevel Stokes-vector modulated signal by polarization-analyzing circuit on InP," *J. Lightw. Technol.*, vol. 36, no. 2, pp. 187–194, Jan. 2018.

- [38] T. Hoang et al., "Enabling high-capacity long-reach direct detection transmission with QAM-PAM Stokes vector modulation," *J. Lightw. Technol.*, vol. 36, no. 2, pp. 460–467, Jan. 2018.
- [39] T. Tanemura and Y. Nakano, "Compact InP Stokes-vector modulator and receiver circuits for short-reach direct-detection optical links," *IEICE Trans. Electron.*, vol. E101.C, pp. 594–601, Jul. 2018.
- [40] M. Morsy-Osman, M. S. Alam, K. A. Shahriar, S. Lessard, and D. V. Plant, "Optimum three-dimensional constellations for Stokes vector direct detect receivers," *IEEE Photon. Technol. Lett.*, vol. 31, no. 8, pp. 587–590, Apr. 2019.
- [41] S. Ghosh, T. Suganuma, S. Ishimura, Y. Nakano, and T. Tanemura, "Complete retrieval of multi-level Stokes vector signal by an InP-based photonic integrated circuit," *Opt. Exp.*, vol. 27, Nov. 2019, Art. no. 36449.
- [42] S. Ishimura, K. Nishimura, Y. Nakano, and T. Tanemura, "Polarization-diversity Stokes-analyzer-based coherent receiver," *Opt. Exp.*, vol. 27, Mar. 2019, Art. no. 9071.
- [43] N. Cui et al., "Joint blind equalization of CD and RSOP using a time-frequency domain Kalman filter structure in Stokes vector direct detection system," Opt. Exp., vol. 27, Apr. 2019, Art. no. 11557.
- [44] K. Kikuchi, "Sensitivity analysis of optically preamplified Stokes-vector receivers using analytically derived formulae for bit-error rate," *Opt. Exp.*, vol. 28, Aug. 2020, Art. no. 26007.
- [45] T. Tanemura, T. Suganuma, and Y. Nakano, "Sensitivity analysis of photonic integrated direct-detection Stokes-vector receiver," *J. Lightw. Technol.*, vol. 38, no. 1, pp. 447–456, Jan. 2020.
- [46] J. Huo et al., "Theoretical and numerical analyses for PDM-IM signals using Stokes vector receivers," Sci. China Inf. Sci., vol. 63, pp. 1–9, Sep. 2020.
- [47] Y. Jin et al., "Adaptive blind Stokes-space based equalizer for RSOP in SV-DD systems with high chromatic dispersion tolerance," *IEEE Photon. J.*, vol. 12, no. 2, pp. 1–13, Apr. 2020.
- [48] M. Nazarathy and E. Simony, "Generalized Stokes parameters shift keying approach to multichip differential phase encoded optical modulation formats," Opt. Lett., vol. 31, Jan. 2006, Art. no. 435.
- [49] M. Nazarathy and E. Simony, "Stokes space optimal detection of multidifferential phase and polarization shift keying modulation," *J. Lightw. Technol.*, vol. 24, no. 5, pp. 1978–1988, May 2006.
- [50] M. Nazarathy and E. Simony, "Error probability performance of equi-energy combined transmission of differential phase, amplitude, and polarization," *J. Lightw. Technol.*, vol. 25, no. 1, pp. 249–260, Jan. 2007.
- [51] P. Perrone, S. Betti, and G. Rutigliano, "Multidimensional modulation in optical fibers," Res. J. Opt. Photon., vol. 2, no. 1, 2018.
- [52] S. Ziaie et al., "Adaptive Stokes-based polarization demultiplexing for long-haul multi-subcarrier systems," *IEEE Photon. Technol. Lett.*, vol. 31, no. 10, pp. 759–762, May 2019.
- [53] H. Ji et al., "High-dimensional Stokes vector direct detection over few-mode fibers," Opt. Lett., vol. 44, Apr. 2019, Art. no. 2065.
- [54] M. D. Feuer, M. V. Bnyamin, and X. Jiang, "Spectral-slicing noise in polarization-modulated optical links," *J. Opt. Commun. Netw.*, vol. 12, no. 4, pp. B55–B62, Apr. 2020.
- [55] M. Visintin, G. Bosco, P. Poggiolini, and F. Forghieri, "Adaptive digital equalization in optical coherent receivers with Stokes-space update algorithm," *J. Lightw. Technol.*, vol. 32, no. 24, pp. 4759–4767, Dec. 2014.
- [56] F. V. Caballero, F. Pittalá, G. Goeger, M. Wang, Y. Ye, and I. T. Monroy, "Novel equalization techniques for space division multiplexing based on Stokes space update rule," *Photonics*, vol. 4, Feb. 2017, Art. no. 12.
- [57] G. M. Fernandes, N. J. Muga, and A. N. Pinto, "Space-demultiplexing based on higher-order Poincaré spheres," *Opt. Exp.*, vol. 25, Jan. 2017, Art. no. 3899.
- [58] D. Che, C. Sun, and W. Shieh, "Optical field recovery in Stokes space," J. Lightw. Technol., vol. 37, no. 1, pp. 451–460, Jan. 2019.
- [59] R. A. Eltaieb et al., "Modulation format identification of optical signals: An approach based on singular value decomposition of Stokes space projections," *Appl. Opt.*, vol. 59, Jul. 2020, Art. no. 5989.
- [60] M. Wen et al., "A survey on spatial modulation in emerging wireless systems: Research progresses and applications," *IEEE J. Sel. Areas Commun.*, vol. 37, no. 9, pp. 1949–1972, Sep. 2019.
- [61] T. A. Eriksson, P. Johannisson, B. J. Puttnam, E. Agrell, P. A. Andrekson, and M. Karlsson, "k-over-L multidimensional position modulation," J. Lightw. Technol., vol. 32, no. 12, pp. 2254–2262, Jun. 2014.

- [62] B. J. Puttnam et al., "Modulation formats for multi-core fiber transmission," *Opt. Exp.*, vol. 22, Dec. 2014, Art. no. 32457.
- [63] B. Puttnam et al., "Energy efficient modulation formats for multi-core fibers," in *Proc. IEEE OptoElectronics Commun. Conf. Australian Conf.* Opt. Fibre Technol., 2014, pp. 694–696.
- [64] B. J. Puttnam et al., "High capacity transmission systems using homogeneous multi-core fibers," *J. Lightw. Technol.*, vol. 35, no. 6, pp. 1157–1167, Mar. 2017.
- [65] C. Fuchs, M. Hoang, and B. Stacey, "The SIC question: History and state of play," Axioms, vol. 6, 2017, Art. no. 21.
- [66] I. Roudas, J. Kwapisz, and E. Fink, "Mode vector modulation," in *Proc. Eur. Conf. Opt. Commun.*, 2021, Paper Tu2D.5.
- [67] E. Fink, J. Kwapisz, and I. Roudas, "Optimized SVM constellations for SDM fibers," in *Proc. IEEE Photon. Conf.*, 2021, Paper TuE3.2.
- [68] J. Kwapisz, I. Roudas, and E. Fink, "Error probability of mode vector modulation optically-preamplified direct-detection receivers," in *Proc. Conf. Lasers Electro- Opt.*, 2022, Paper SM4J.1.
- [69] J. Kwapisz, I. Roudas, E. Fink, and A. Biswas, "Mode vector modulation direct-detection receivers with linear hardware complexity," in *Proc. IEEE Photon. Conf.*, 2022, Paper TuF1.3.
- [70] J. Kwapisz, I. Roudas, and E. Fink, "Polarimetric direct detection for spatial superchannels," in *Proc. IEEE Asia Commun. Photon. Conf.*, 2022, pp. 670–673.
- [71] I. Roudas, J. Kwapisz, and E. Fink, "Mode vector modulation: A review," in *Proc. IEEE 23rd Int. Conf. Transparent Opt. Netw.*, 2023, Paper We.D2.3.
- [72] C. Antonelli, A. Mecozzi, M. Shtaif, and P. J. Winzer, "Stokes-space analysis of modal dispersion in fibers with multiple mode transmission," *Opt. Exp.*, vol. 20, no. 11, pp. 11718–11733, 2012.
- [73] I. Roudas and J. Kwapisz, "Stokes space representation of modal dispersion," *IEEE Photon. J.*, vol. 9, no. 5, pp. 1–15, Oct. 2017.
- [74] I. Roudas, J. Kwapisz, and D. A. Nolan, "Optimal launch states for the measurement of principal modes in optical fibers," *J. Lightw. Technol.*, vol. 36, no. 20, pp. 4915–4931, Oct. 2018.
- [75] J. P. Gordon and H. Kogelnik, "PMD fundamentals: Polarization mode dispersion in optical fibers," *Proc. Nat. Acad. Sci.*, vol. 97, pp. 4541–4550, 2000.
- [76] T. Hayashi, Y. Tamura, T. Hasegawa, and T. Taru, "Record-low spatial mode dispersion and ultra-low loss coupled multi-core fiber for ultralong-haul transmission," *J. Lightw. Technol.*, vol. 35, no. 3, pp. 450–457, Feb. 2017.
- [77] K. Yoshida, T. Fujisawa, T. Sato, and K. Saitoh, "Optimum index profile of few-mode coupled multicore fibers for reducing the group delay spread" Opt. Exp., vol. 27, pp. 16281–16295, May 2019.
- spread," *Opt. Exp.*, vol. 27, pp. 16281–16295, May 2019.

 [78] Corning Inc., Corning, NY, "Corning SMF-28 Ultra Optical Fiber," Product Information, Nov. 2021.
- [79] K. Kikuchi and S. Kawakami, "16-ary Stokes-vector modulation enabling DSP-based direct detection at 100 Gbit/s," in *Proc. Opt. Fiber Commun. Conf.*, 2014, Paper Th3K.6.
- [80] D. Divsalar and M. Simon, "Multiple-symbol differential detection of MPSK," *IEEE Trans. Commun.*, vol. 38, no. 3, pp. 300–308, Mar. 1990.
- [81] M. L. McCloud and M. K. Varanasi, "Modulation and coding for noncoherent communications," J. VLSI Signal Process. Syst., vol. 30, pp. 35–54, Feb. 2002.
- [82] A. Gil, J. Segura, and N. M. Temme, "Algorithm 939: Computation of the Marcum Q-function," ACM Trans. Math. Softw., vol. 40, no. 3, 2014, Art. no. 20.
- [83] N. M. Temme, "Asymptotic and numerical aspects of the noncentral chi-square distribution," *Comput. Math. Appl.*, vol. 25, no. 5, pp. 55–63, 1993.
- [84] N. M. Temme, "A double integral containing the modified Bessel function: Asymptotics and computation," *Math. Comput.*, vol. 47, no. 176, pp. 683–691, 1986.
- [85] S. Goldstein, "On the mathematics of exchange processes in fixed columns. I. Mathematical solutions and asymptotic expansions," *Proc. Roy. Soc. London Ser. A*, vol. 219, pp. 151–171, 1953.
- [86] G. J. Foschini, R. D. Gitlin, and S. B. Weinstein, "Optimization of twodimensional signal constellations in the presence of Gaussian noise," *IEEE Trans. Commun.*, vol. 22, no. 1, pp. 28–38, Jan. 1974.
- [87] M. Karlsson and E. Agrell, "Multidimensional optimized optical modulation formats," in *Enabling Technologies for High Spectral-Efficiency Coherent Optical Communication Networks*, X. Zhou and C. Xie, Eds. Hoboken, NJ, USA: Wiley, 2016, ch. 2, pp. 13–64.
- [88] S. Boyd, S. P. Boyd, and L. Vandenberghe, Convex Optimization. Cambridge, U.K.: Cambridge Univ. Press, 2004.

- [89] Wikipedia Contributors, "Thomson problem-Wikipedia, the free encyclopedia," 2023. Accessed: Nov. 28, 2023. [Online]. Available: https://en.wikipedia.org/w/index.php?title=Thomson_problem
- [90] E. B. Saff and A. B. Kuijlaars, "Distributing many points on a sphere," *Math. Intelligencer*, vol. 19, no. 1, pp. 5–11, 1997.
- [91] D. J. Wales and S. Ulker, "The Cambridge cluster database: Global minima for the Thomson problem," Accessed: Nov. 28, 2023. [Online]. Available: https://www-wales.ch.cam.ac.UK/~wales/CCD/ Thomson/table.html
- [92] J. Kogan, "A new computationally efficient method for spacing n points on a sphere," *Rose-Hulman Undergraduate Math. J.*, vol. 18, no. 2, 2017, Art. no. 5.
- [93] J. Jasper, E. J. King, and D. G. Mixon, "Game of Sloanes: Best known packings in complex projective space," *Proc. SPIE*, vol. 11138, pp. 416–425, 2019.
- [94] E. J. King, "Game of Sloanes," Accessed: Nov. 28, 2023. [Online]. Available: https://www.math.colostate.edu/~king/GameofSloanes.html

- [95] E. Agrell, J. Lassing, E. Ström, and T. Ottosson, "Gray coding for multilevel constellations in Gaussian noise," *IEEE Trans. Inf. Theory*, vol. 53, no. 1, pp. 224–235, Jan. 2007.
- [96] M. R. Garey and D. S. Johnson, Computers and Intractability: A Guide to the Theory of NP-Completeness. San Francisco, CA, USA: W. H. Freeman, 1979.
- [97] S. Sahni and T. Gonzalez, "P-complete approximation problems," J. ACM, vol. 23, pp. 555–565, Jul. 1976.
- [98] S. Kirkpatrick, C. D. Gelatt, and M. P. Vecchi, "Optimization by simulated annealing," *Science*, vol. 220, no. 4598, pp. 671–680, 1983.
- [99] F. Gray, "Pulse code communication," U.S. Patent 2632058, Mar. 17, 1953.
- [100] P. A. Humblet and M. Azizoglu, "On the bit error rate of lightwave systems with optical amplifiers," *J. Lightw. Technol.*, vol. 9, no. 11, pp. 1576–1582, Nov. 1991.
- [101] S. Benedetto, E. Biglieri, and V. Castellani, *Digital Transmission Theory*. Englewood Cliffs, NJ, USA: Prentice-Hall, 1987.